Evaluation of Turbulence Models for Predicting Entropy Generation in Bypass-Transitional Boundary Layers

A Thesis

Presented in Partial Fulfillment of the Requirements for the

Degree of Master of Science

with a

Major in Mechanical Engineering

in the

College of Graduate Studies

University of Idaho

by

Joseph George

Major Professor: Tao Xing, Ph.D.

Committee Members: Ralph Budwig, Ph.D.; John Crepeau, Ph.D.

Department Administrator: Steven Beyerlein, Ph.D.

July 2015

Authorization to Submit Thesis

This thesis of Joseph George, submitted for the degree of Master of Science with a Major in Mechanical Engineering and titled "**Evaluation of Turbulence Models for Predicting Entropy Generation in Bypass-Transitional Boundary Layers,**" has been reviewed in final form. Permission, as indicated by the signatures and dates below, is now granted to submit final copies to the College of Graduate Studies for approval.

Major Professor _____Date_____
Tao Xing, Ph.D.

Committee Members _____Date_____
John Crepeau, Ph.D.

_____Date_____
Ralph Budwig, Ph.D.

Department Administrator _____Date_____
Steven Beyerlein, Ph.D.

Abstract

The primary objective of this study is to evaluate the accuracy of using turbulence models to predict entropy generation rates in bypass transitional flows under various pressure gradients in a spatially growing boundary layers over a flat plate. Entropy generation rates in such flows are evaluated using CFD methods. Various turbulence models are assessed by comparing results with DNS data and two recent CFD studies. 3D bypass transition simulations are also performed using LES and IDDES models. Results show better agreement with DNS than any previous RANS studies. The k-ω 4eqn. transition model shows closest agreement to DNS data for 2D flow. The SGS models are highly dissipative and LES will require much finer grid within boundary layer region and freestream. These models fail to predict bypass-transition accurately due to lack accurate unsteady fluctuations and grid resolution. Certain limitations and issues are identified and recommendation are made for future studies.

Acknowledgements

Immeasurable appreciation and deepest gratitude for all the help and support are extended to the following persons who in one way or another have contributed in making this study possible.

First and foremost a special thanks to my advisor **Dr. Tao Xing** for his support, advices, guidance that benefited much in the completion and success of this study. **Dr. John Crepeau** and **Dr. Ralph Budwig** for serving on the committee, their valuable comments, suggestions and provisions.

The author would also like to recognize the support of Dr. Sean Quallen, Mr. Jose Ramirez and Ms. Huijin Zhang for sharing their knowledge and endless help during my time at the University of Idaho.

This work was supported by the **U.S. Department of Energy, Office of Science, Basic Energy Sciences, under Award # DE-SC0004751**. The authors would also like to thank Dr. Donald McEligot, Dr. Tamer Zaki, Dr. Kevin Nolan, and Dr. Edmond Walsh for meaningful contributions.

Dedication

This work is dedicated to my parents, my sister and all my dear friends for their continual support, untiring patience, understanding and most of all their love throughout my life.

Table of Contents

List of Figures

List of Tables

Nomenclature

$\langle \_ \rangle =$ Profile averaged quantity

$\{ \_ \} =$ Function

$\| \_ \|_2 =$ L2 norm

$| \_ | =$ Absolute value

$\overline{(\_)} =$ Time averaged quantity

$A\{x\} =$ Cross-sectional area, m^2

$h\{x\} =$ Height in plate-normal direction, m

$k =$ Turbulent kinetic energy, $\frac{\overline{u'^2} + \overline{v'^2} + \overline{w'^2}}{2}$, m^2/s^2

$L_x, L_y, L_z =$ Length in the streamwise, plate-normal, and span-wise directions, respectively, m

$n_x, n_y, n_z =$ Number of grid points in the streamwise, plate-normal, and span-wise directions, respectively

$P =$ Distance metric to the asymptotic range

$p =$ Pressure, Pa

$\langle p_G \rangle =$ Profile averaged order of accuracy

$p_{th} =$ Theoretical order of accuracy

$Q =$ Volumetric flow rate, m^3/s

$q^2 =$ Sum of velocity fluctuations squared, $u'^2 + v'^2 + w'^2$, m^2/s^2

$\langle R_G \rangle =$ Profile averaged convergence ratio

$r_G =$ Grid refinement ratio, $\Delta x_{G_2} / \Delta x_{G_1}$ and $\Delta x_{G_3} / \Delta x_{G_2}$

$S_{ij} =$ Strain tensor, $\frac{1}{2}\left(\frac{\partial u_i}{\partial x_j} + \frac{\partial u_j}{\partial x_i} \right)$

$S_T =$ Strain rate magnitude, $\sqrt{2 S_{ij} S_{ij}}$

$S_{\#} =$ Value of a given variable with the grid refinement specified in the subscript

$S'', S''' =$ Entropy generation rate per unit surface area and pointwise entropy generation rate, respectively, kg/K-s^3 and kg/K-m-s^3

$T =$ Temperature, K

$U, u =$ Mean velocity and velocity component in the *x* direction, respectively, m/s

$U_G =$ Grid uncertainty

$u_\tau =$ Friction velocity, $\sqrt{\tau_w / \rho}$, m/s

$u', v', w' =$ Velocity fluctuations in the *x*, *y*, and *z* directions, respectively, m/s

$\overline{u_i' u_j'} =$ Mean fluctuation product in Reynolds shear stress, m^2/s^2

$V, v =$ Mean velocity and velocity component in the *y* direction, respectively, m/s

$W =$ Velocity component in the *z* direction, m/s

$x, y, z =$ Coordinates in the streamwise, plate-normal, and span-wise directions, respectively

Non-Dimensional Quantities

$C_d =$ Dissipation coefficient, $\dfrac{TS''}{\rho U_{\text{fs}}^3\{x\}}$

$C_{\text{f}} =$ Skin friction coefficient, $\dfrac{\tau_w}{\rho U_{\text{fs}}^2\{x\}}$

$C_s =$ Correlation constant

$E_s =$ Correlation exponent

$H\{\lambda\} =$ Shape factor correlation function, $\dfrac{\delta^*}{\theta}$

$Re_{(\_)} =$ Reynolds number with corresponding subscript, $\dfrac{(\_)U_{\text{fs}}\{x\}}{\nu}$

$S\{\lambda\} =$ Wall shear stress correlation function, $\dfrac{\tau_w\theta}{\mu U_{\text{fs}}\{x\}}$

$\left(S''\right)^+ =$ Entropy generation rate per unit surface area, $\dfrac{TS''}{\rho u_\tau^3}$

$\left(S'''\right)^+ =$ Pointwise volumetric entropy generation rate, $\dfrac{T\nu S'''}{\rho u_\tau^4}$

$U^+ =$ Mean velocity, $\dfrac{U}{u_\tau}$

$x^+ =$ Streamwise coordinate, $\dfrac{xu_\tau}{\nu}$

$y^+ =$ Wall-normal coordinate, $\dfrac{yu_\tau}{\nu}$

Greek Symbols

$\beta =$ Streamwise pressure gradient parameter, $\frac{2m}{1+m}$

$\Delta x, \Delta y, \Delta z =$ Grid sizes in the x, y, and *z* directions, respectively, m

$\Delta x^+, \Delta y^+ \Delta z^+ =$ Non-dimensional grid sizes in the x, y, and *z* directions, respectively

$\Delta t^+ =$ Non-dimensional step size, $\frac{U_{\text{fs}} \Delta t}{\delta_0}$

$\delta, \delta^* =$ Boundary layer thickness and displacement thickness, respectively, m

$\delta_{\%} =$ Percentage difference; $\delta_{RE} =$ Error estimate

$\varepsilon =$ Turbulent dissipation rate, m^2/s^3

$\varepsilon_{\#\#} =$ Change between $\hat{S}_{\#}$ for different grids, example, $\varepsilon_{21} = \hat{S}_2 - \hat{S}_1$

$\gamma =$ Intermittency based on C_{f}

$\eta =$ Similarity parameter from Blasius solutions

$\mu =$ Absolute viscosity, kg/m-s

$\mu_t =$ Absolute turbulent viscosity, $\rho \nu_t$

$\omega =$ Specific turbulence dissipation rate, 1/s

$\theta =$ Momentum thickness, m

$\nu =$ Kinematic viscosity, μ / ρ, m^2/s

$\nu_t =$ Turbulent viscosity, m^2/s

$\rho =$ Density, kg/m^3

$\tau =$ Wall shear stress, $\mu \left. \frac{\partial u}{\partial y} \right|_{y=0}$

Superscripts and Subscripts

$(\_)^{+}$ = Normalization by wall units

$\_', \_'', \_'''$ = First, second, and third derivatives, respectively

$1, 2, 3$ = Corresponds to the fine, medium, or coarse grid, respectively

fs = Freestream

i, j, k = Represents variables corresponding to one of the three directions, *x*, *y*, or *z*, independently.

L = Length of the plate

0 = Value at the inlet

Abbreviations

CFD = Computational Fluid Dynamics

ZPG = Zero Pressure Gradient

APG = Adverse Pressure Gradient

FPG = Favorable Pressure Gradient

DNS = Direct Numerical Simulations

RANS = Reynolds Averaged Navier Stokes

LES = Large Eddy Simulations

IDDES = Improved Delayed Detached Eddy Simulations

SST = Shear Stress Transport

RSM = Reynolds Stress Model

TKE = Turbulent Kinetic Energy

HVAC = Heating, Ventilation and Air-Conditioning

Chapter 1: Introduction and Background

1.1 Entropy Generation in Boundary Layers

Entropy is a state function in any system. The generation of entropy provides a measure of irreversibility of the process or can be expressed as the disorder or randomness of system. Irreversibility or entropy generation is directly related to the loss of available work. The concept of availability and exergy destruction go hand in hand with the concept of entropy generation and have a series of characteristic features encountered in irreversible systems and processes. By its definition, lost available work is zero if and when a system operates reversibly while in the irreversible case, it is always a positive quantity. Therefore, lost available work or entropy generated in a system is a measure of the degree of thermodynamic irreversibly of that system. The work 'available' indicates that the system irreversibility is responsible for the one-way destruction of an amount of work that would otherwise be available for use [1].

Four different mechanisms contribute to the generation of entropy: Mean and fluctuating heat fluxes as well as the mean and fluctuating viscous effects. The viscous effect of a fluid is responsible in creating a boundary layer over the surface of a body. The boundary layer is susceptible to both the net heat flux and the viscous effects of the flow and the body. Therefore, the mechanisms responsible for entropy generation are pertinent and have maximum impact in the boundary layer region.

In case of a steady, unheated, laminar flow, there are no heat flux effects and the fluctuations in viscous effects are zero. Therefore, the entropy generation occurs only from the viscous losses associated with mean velocity gradients within the boundary layer. Bypass transition is different than natural transition to turbulence. Bypass transition is induced in a

flow where the freestream vortical disturbances cause the boundary layer to transition to turbulence earlier and without the intervention of viscous Tollmien-Schlichting waves [2] that are responsible for natural transition. An unheated bypass transitional boundary layer flow is characterized by viscous losses associated with the mean and fluctuating velocity gradients, thereby, resulting in entropy generation within the bypass transitional boundary layer.

1.1.1 Importance of Minimizing and Controlling Entropy Generation

Entropy generation is the property of a system that serves as the measure of irreversibility or the loss of available work within a system. The mechanisms for the generation of entropy are related to heat flux and viscous effects. These are two most important characteristic features of any fluid flow system. Some examples of systems that involve fluid flow physics include: nuclear reactors, thermal heat exchangers, HVAC systems, cooling system of electronic devices, exhaustible and sustainable power generation techniques and many more. All such flow systems subjected to heat flux and viscous effects which would directly contribute to the higher entropy generation in these flow systems. A higher entropy generation would lead to a higher irreversible loss of energy from a fluid flow system. Determining and minimizing entropy generation within a flow would help reduce the loss of energy and thereby, improve the overall efficiency of the system [3]. In order to initiate studies into effective means of minimizing and controlling the entropy generation process; we need to first and foremost gain a fundamental understanding of the characteristics and physics that lead to the generation of entropy within boundary layer and identify efficient methods to quantitatively and qualitatively measure them within the boundary layer.

1.1.2 Objective and Applications

The objective of the current study is to evaluate the accuracy of various turbulence models to predict entropy generation and location of transition within a bypass transitional boundary layer. The commercial CFD software ANSYS FLUENT is employed for simulations. The flow modeled with RANS turbulence model is steady, incompressible, two-dimensional bypass transitional boundary layer flow. The RANS models employed in the study are the k-ε model, k-ω SST model, RSM model and transitional 4 equation SST k-ω model. Quantitative solution verification is conducted using three systematically refined structured grids, with the finest grid containing about 1 million grid points. The flow characteristics are compared to the DNS results from Nolan and Zaki [4] and two recent CFD studies.

The results from this study will provide a better understanding of the effectiveness of employing RANS / LES methodologies in contrast to other methods for conducting entropy generation studies in transitional and turbulent boundary layer flows. The knowledge thus gained regarding such strategies will result in efficient use of current resources available for entropy generation studies and provide direction to future studies in minimizing entropy generation rates and such applications.

1.2 Background

A literature review is performed to depict different approaches employed in the study of boundary layer entropy generation and the extents of these studies are detailed here.

1.2.1 Analytical Methods and Experimental Studies

Analytical methods are a common means to scientific studies. However, most analytical studies require considerable simplification of the problem and corresponding

assumptions. The use of analytical approaches in the study of boundary layer entropy generation are limited to laminar and steady flow solutions. This is particularly due to the fact that analytical studies only take into account the mean velocity and heat flux entropy generation mechanisms. Ozkol and Arikoglu [5] derived an equation for the minimization of total entropy generation by analyzing natural convection of laminar flow over a vertical wall of constant temperature. Similarly, Esfahani and Jafarian [6] studied and compared three different methods of predicting entropy generation: an integral solution, a similarity solution and a Blasius series solution for total entropy generation rates in a zero pressure gradient, flat plate laminar boundary layer over a constant temperature vertical wall. Application of analytical strategies for analyzing bypass transitional boundary layer flows are largely deemed insufficient due to the fact that transitional boundary layers are inherently unsteady.

In any field of science and engineering, experimental studies are extremely important to develop an understanding the natural behavior and state of any phenomenon and the physics associated with that behavior. Therefore, experimental verification strategies and their application are paramount in the study of boundary layer entropy generation. However, in case of transitional and turbulent boundary layer studies, which are inherently unsteady, sampling transient characteristics of such flows makes entropy generation measurement and approximation extremely difficult in experimental studies. In order to overcome these difficulties, experimental researchers employ a variety of data sampling strategies: non-conditional sampling, laminar-conditioned, turbulent-conditioned, and an intermittency weighted technique, which is a combination of the two conditionally sampled methods.

Walsh et al. [7] conducted an experimental study involving a transitional flow over a flat plate with a zero pressure gradient and a favorable pressure gradient (with $\beta = 0.27$) with

$Re_\theta \leq 500$. The study analyzed these experimental measurements and compared the entropy generation approximations from the different transient flow sampling methodologies. The study concluded that the intermittency-weighted data predictions were 20% lower than the non-conditionally sampled data for low Reynolds numbers. A separate study by Nolan et al. [8] analyzed experimental results to develop a semi-empirical technique for predicting entropy generation in transitional boundary layers with zero and favorable pressure gradients. Adeyinka and Naterer [9, 10] conducted a particle image velocimetry (PIV) study of turbulent flows within a channel. The experiment involved flows with Reynolds numbers based on friction velocity, Re_{u_τ}, from 187-399. The study demonstrated a 3% deviation from the results of White [11]. This study also compared the data with direct numerical simulations to confirm that the turbulent entropy production was modeled correctly.

Skifton et al. [12, 13] conducted experimental measurements for entropy generation within bypass transitional flow at the Matched Index of Refraction (MIR) flow facility at the Idaho National Laboratory on a submerged flat plate made from quartz. The study employed PIV techniques to capture spatial vector maps at near wall location with five to ten points within the viscous sub layer. The study aimed at directly calculation entropy generation from the measured velocity fluctuation derivatives and predict the onset of transitional flow from the calculated pointwise entropy.

1.2.2 Direct Numerical Simulation (DNS)

Direct numerical simulation (DNS) is a numerical analysis technique. DNS simulates and completely resolves all of the laminar and turbulent length scales and thus can be used as a numerical benchmark to evaluate the accuracy of simulations using various turbulence models. DNS has been proven to be an extremely accurate and effective tool in elucidating

complex flow physics associated with phenomena that are extremely difficult to experimentally measure and control. McEligot et al. [7, 14] analyzed DNS results from two different studies conducted by Spalart [15, 16] of turbulent boundary layer flows with zero and favorable pressure gradients with Re_θ, ranging from 300 to 1410. The study showed that the methodology developed by Rotta [17] for approximating S‴ is inaccurate for the given flow characteristics since the study found that approximately two-thirds of the entropy generation occurs in the viscous layer of a turbulent boundary layer (defined as $y+ \approx 30$). The study demonstrated that entropy dissipation is nearly universal within the viscous layer of turbulent boundary layer flows with zero and favorable pressure gradients. This has been recently elucidated by a RANS study for zero and favorable gradients by Ghasemi et al. [18, 19]. McEligot et al. [20] similarly analyzed results from a DNS [21] of turbulent channel flow with zero and favorable pressure gradients. McEligot compared two methods for determining entropy generation. The first method evaluated the fluctuating gradients forming the dissipation term in the turbulent enthalpy equation and the second method evaluated an approximate analogy to laminar flow employing assumed boundary layer (and other) approximations [22]. Both methods predict similar S″ values. The second method under-predicted entropy generation in the "linear" layer and over-predicted entropy generation in the rest of the viscous layer.

Another study by McEligot et al. [23] compared the entropy generation predicted from a DNS of turbulent boundary layer flow to the entropy generation predicted from a DNS of channel flow[21, 24]. The study demonstrated that the pointwise entropy generation at the boundary of the viscous layer is relatively insensitive for both boundary layer and channel flows with large favorable pressure gradients. The integral over the area of the viscous layer

decreased moderately only for boundary layer flows. Walsh and McEligot [25] improved an existing correlation for the dissipation coefficient, C_d, using data from multiple DNS studies of low Re_θ turbulent boundary layer and channel flows with zero and favorable pressure gradients [15, 21, 26, 27]. Walsh et al. [3] analyzed a DNS of bypass transitional boundary layer flows for Re_θ ranging from 115 to 520 [28, 29]. The study demonstrated that the term for turbulent convection in the turbulent kinetic energy (TKE) balance is significant within the transition region. This is as a consequence of more turbulent energy being produced than dissipated. The study showed that a popular approximation method over-estimates the dissipation coefficient by as much as 17%. The study demonstrated that the approach developed by Rotta [17] is more accurate for transitional boundary layers.

A DNS of bypass transition was performed by Zaki and Durbin [2]. This simulation showed that high-frequency, freestream fluctuations are kept from entering the boundary layer due to "shear sheltering." The study evaluated the coupling coefficient between continuous spectrum Orr-Somerfield and squire modes. The study demonstrated that a strongly and weakly coupled high-frequency mode is required to simulate the transition process completely. The bypass transition simulations here are compared to a DNS by Nolan and Zaki [4]. The DNS study used a computational domain size of $(Lx, Ly, Lz)/\delta 0 = (900, 40, 30)$ with a grid resolution of $(nx, ny, nz) = (3072, 192, 192)$. The spatial resolution was $(\Delta x+, \Delta y+, \Delta z+) = (11.7, \geq 0.40, 6)$. The inlet mean velocity Blasius profile was created based on $Re_{\delta 0} = 800$ with a turbulent intensity of 3%. The study tracked down turbulent spots resulting from high-amplitude streaks upstream. The study found that the volumetric growth rate of turbulent spots is insensitive to the pressure gradient. The current study evaluates all its data against that from the DNS study by Nolan and Zaki [4].

1.2.3 RANS Model Simulations

As mentioned earlier, two recent CFD studies by Ghasemi et al. [18, 19] aimed at evaluating the accuracy of different turbulence and transitional RANS models in predicting boundary layer behavior and entropy generation in bypass transition, including the k-ε model, the SST k-ω model, the k-ω 4 equation model, the k-kl-ω 3-equation model, and the Reynolds stress model (RSM).

The study used a relatively coarse mesh containing 149,089 grid points on a two-dimensional, zero pressure gradient domain corresponding to $Lx/\delta_0 = 900$ in the streamwise direction and an adverse pressure gradient domain equal to $Lx/\delta_0 = 600$ in the streamwise direction. The inlet boundary condition was specified with a turbulence intensity $\left(I = u'/U ; u' = \sqrt{2k/3}\right)$ of 3% and a turbulent length scale equal to the boundary layer thickness at the inlet.

These studies showed that the RANS models predicted the onset of transition much earlier than compared to the corresponding cases in the DNS study [4]. The RANS models employed in these also over-predicted the integral entropy generation rate and the skin friction coefficient in the transition region.

Owen [30] also conducted similar RANS model studies for the zero pressure gradient case with much finer grid resolution and compared it to Ghasemi and the DNS data. The study showed significant improvement in the prediction of transition onset compared to Ghasemi [18]. However, it was noted that the inlet turbulence levels simulated by Owen were considerably lower than that from the DNS and RANS simulations. Also, both the RANS studies mentioned here were evaluated in 2D alone and 3D comparisons to the DNS study were not evaluated.

1.2.4 Large Eddy Simulations (LES)

LES models resolve the majority of the turbulence energy spectrum and only model the sub-grid scales. Therefore, LES models are more frequently being implemented in CFD research due to the fact that it resolves all the larger and most turbulence length scales and better represents the actual turbulence physics unlike RANS solutions which only resolves the mean flow and completely models all scales of turbulence. Employing LES methods will usually lead to more accurate solutions over RANS models but with a lower computational cost than DNS. Therefore, it may be looked at as a compromise with better accuracy and lower cost. Numerous LES sub-grid scale (SGS) models have been developed in recent times, allowing researchers to cater the LES model to better capture the physics of the flow. These existing LES models are continually being refined for different applications and even more models being developed. LES is relatively a newer approach in CFD studies. Application of LES techniques to boundary layer studies have been quite limited in the past.

Lardeau et al. [31] employed LES and focused on unsteady boundary layer processes before, during, and after bypass transitional boundary layer flow over a flat plate. The inflow conditions were based on $Re_\theta = 425$ with three different inlet turbulent intensities: 2.5%, 4.3%, and 8%. The study applied the localized Lagrangian-averaged dynamic eddy-viscosity SGS model. The study demonstrated how the pre-transitional, elongated, streaky structures led to the amplification of fluctuations by conventional shear-stress/shear-strain interaction instead of by pressure diffusion. The study noted that uncertainties arise from the lack of realism in the free-stream conditions.

Another study by Lardeau et al. [32] compared the ability of different SGS models to predict separation bubbles in transitional flow over both, a flat plate and a compressor blade.

The chord length of the compressor blade was specified as the reference length, L_c. The inflow conditions were Re_{Lc} = 60,000 and Re_{Lc} = 138,500 for the flat plate and compressor blade, respectively. The inflow turbulent intensities were 0%, 1%, 1.5%, and 2% for the flat plate and 0% and 3.25% for the compressor blade.

The study applied the Smagorinsky-Lilly dynamic model, the mixed-time-scale model, and the wall-adapted local eddy viscosity (WALE) model to represent the SGS processes. The study showed that results from all three SGS models are consistent with previous theoretical and numerical analyses for the flat plate geometry. For the compressor blade geometry, only the mixed-time-scale model returned a fair representation of both pressure and skin friction following separation. The study also demonstrated that the sensitivity of the results to the SGS model decreased as the inlet turbulent intensity increased.

Monokrousos et al. [33] applied a linear model-based feedback control to delay the onset of transition in bypass transitional flows over a flat plate. The inflow conditions were based on $Re_{\delta*}$ = 300 with an inlet free-stream turbulent intensity of 4.7%. The study demonstrated that the control mechanism was successfully able to reduce the energy of the streaks, preventing the streaks from diffusing into the shear layer near the wall, subsequently delaying the onset of transition. A study by Sheikhi et al. [34] employed a modification to a filtered density function (FDF) model to determine the entropy generation in turbulent mixing layer flows. The FDF model was modified to close the filtered entropy transport equation with a system of stochastic differential equations. The flow was characterized by two parallel streams of equal velocities entering the domain in opposite directions. A fourth-order scheme was applied for the spatial and time discretization. The study demonstrated that the modifications to the FDF model agree with the DNS data from Huai et al. [35].

In order to accurately capture the flow physics, the LES time and length scales must be sufficiently small. The smallest length scale is the Kolmogorov scale where the viscous dissipation takes place. Since the grid size relates to the filter size, a certain grid size is necessary to capture the energy within different wavenumbers. Ferziger [36] notes that a second-order numerical discretization scheme cannot compute the derivatives of modes with wavenumbers higher than $k_{max}=\pi/2\Delta x$, where k_{max} is the maximum wavenumber of the Fourier modes. This means that most of the energy should be contained at wavenumbers below k_{max}. Kornhaas et al. [37] considered a test case to determine the appropriate time step size and convergence criterion per time step for a periodic flow over a two-dimensional hill. A second-order central difference scheme applied spatially and the implicit Crank-Nicolson scheme was applied for time discretization. The study found that LES simulations require a time step corresponding to CFL = 2 with a convergence criterion per time step of 10^{-2}.

Sayadi and Moin [38, 39] studied natural H-type and K-type transition of a flat plate boundary layer using large eddy simulations to predict the skin friction profile through the transitional and turbulent regimes. They study was compared to a pervious DNS study by Sayadi [40] to validate the computations. The study evaluated various dynamic and constant coefficient LES models on two separate grids with 1.2 million and 8 million grid points. The study showed that constant coefficient LES models fail to predict the point of transition accurately due to high rate of dissipation of the linear disturbances in the laminar region. The study showed that by employing Dynamics SGS models, the point of transition can be estimated correctly. The study also concluded that the coarse grid under-predicts the skin friction profile in the transitional and turbulent regime.

In a more recent DNS study, Sayadi, Hamman and Moin [41] show that at this point, computed power spectra exhibit a decade of Kolmogorov inertial subrange; further evidence of convergence to equilibrium turbulence at the late stage of transition. Here, visualization of the instantaneous flow structure shows numerous, tightly packed hairpin vortices [42]. Strongly organized coherent hairpin structures are less perceptible farther downstream (at higher Reynolds numbers), but the flow statistics and near-wall dynamics are the same.

The time and spanwise averaged skin-friction maximum in both H- and K-type transitions overshoots the turbulent correlation. Downstream of these friction maxima, all three skin-friction profiles collapse when plotted versus the momentum-thickness Reynolds number, Re_θ. Mean velocities, turbulence intensities and integral parameters collapse generally beyond Re_θ=900 in each transition scenario. They postulated that these dynamics of late-stage transition as manifested by hairpin packets can serve as a reduced-order model of high-Reynolds-number turbulent boundary layers. The overshoot, and downstream dissipation of the skin-friction profiles was seen in all LES cases tested in the current study.

Building from previous studies and proposed non-equilibrium wall models, Park and Moin [43] recently proposed, implemented and validated an improved dynamic non-equilibrium wall model for Large Eddy Simulations with some major differences. They implemented the new model using an unstructured solver for the first time.

This present wall-model is equipped with a new dynamic correction for the wall-model eddy viscosity/conductivity. Persistent over prediction of the skin friction caused by the addition of the resolved turbulent stress has been a chronic problem for non-equilibrium wall-models. The proposed model senses the local state of the resolved stress and uses this information to dynamically adjust the model coefficients. The model regulates the eddy

viscosity based on the physical and mathematical constraints on the total Reynolds stress in the wall-model, and is dynamic in the sense that the model coefficients are determined automatically from the wall-model solution only, without using any adjustable parameters.

The current study did not use any newly proposed wall modelling for LES simulations. The LES studies here were limited to some combination of available wall treatments, models and delta filters within the commercial CFD software.

1.2.5 Limitations of previous CFD studies and Motivation

CFD studies review in the above section show some important limitations and further provide motivation to carry out the current research. The studies by Gashemi et al. [18, 19] used coarse grid sets and no solution verification was conducted for those studies. Therefore, the grid dependence of the solution is unknown.

Moreover, they used a mean inlet turbulent intensity rather than a more appropriate inlet conditions with turbulent kinetic energy and dissipation rate profiles. The results of these studies are fairly inaccurate when compared to that from the DNS data [4]. The study also does not provide a good understanding of the capability of turbulence models to predict transition in the boundary layer.

In his study of bypass transition, Landon [30] conducted systematic grid refinement studies and used a much finer grid for his simulations. The study also used a more appropriate inlet boundary condition by specifying the turbulent structure profiles. However, the strength of the turbulent profiles specified were significantly lower than actual values obtained from the DNS data. The study mainly focused on entropy generation in laminar boundary layers and only a zero pressure gradient bypass transition case was evaluated.

LES studies applied to natural transition have shown the capability of dynamic models compared to that of constant coefficient models. However, LES methods have not been applied to bypass transitional flows and the ability of such models in predicting bypass transition have not been evaluated.

Past CFD studies have major shortcomings in effectively evaluating various turbulence and transitional RANS models for prediction of bypass transition and entropy generation within a boundary layer, as explained above, and the lack of significant studies into bypass transition employing 3D simulations and different LES models provide two major motivating factors in the current study.

Chapter 2: Simulation Design and Implementation

2.1 Geometry and Grid Generation

In order to effectively evaluate the ability of various turbulence models in predicting the boundary layer transition phenomenon and the corresponding pointwise entropy generation process, all outcomes of this research are compared to that from the DNS study [4]. The 2-dimensional and 3-dimentional geometry used in this study is designed to be exactly the same as that in DNS for the ZPG / APG RANS and the ZPG LES / IDDES cases in the streamwise and normal direction. Therefore, the length of the flat plate, Lx, is the same as the DNS study for the corresponding ZPG and APG flow conditions. The overall streamwise length of the domain (same as the plate) expressed as a ratio to the inlet boundary layer thickness, Lx/δ_0 = 900 and 600 for ZPG and APG cases, respectively. The desired pressure gradients are generated in the flow by employing a curved profile for the top wall surface of the domain.

The geometry and the mesh were created in the commercial meshing software tool Pointwise v17.0R1 on a local workstation. The grid point distribution is uniform in the streamwise and spanwise directions whereas in they are distributed with a growth ratio in the plate-normal direction. This results in clustering a large number of points close to the plate surface and ensures good resolution of the flow field within the boundary layer region to completely capture the large gradients of flow physics near the plate surface. The first grid point placement is such that the y^+ value is below 1.

Three sets of grids were created for all RANS cases with varying total number of discretized grid points. All RANS solution results presented and discussed here are for the fine mesh set containing approximately ~1M grid points. Coarse and medium meshes were

also generated using a constant grid refinement ratio of $2^{1/2}$ and were used to conduct a detailed solution verification and grid dependency study. Figure 2.1 below shows the schematic representation of the geometry and the grid generated for the ZPG and APG cases in the current study.

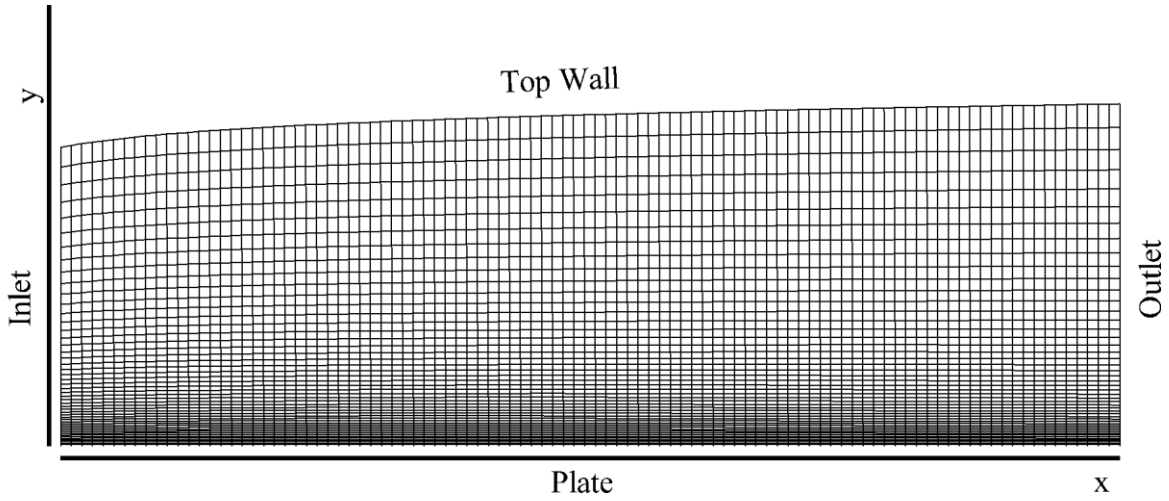

Figure 2.1 Schematic representation of the geometry and mesh

The grid generation process for the 3D LES / IDDES cases is similar in approach. The 2-D grid shown here is extruded in the span wise direction to create a 3-D domain of exactly the same dimensions as that used for DNS. However, the number of grid point, distribution of points vary. Hence, there are some corresponding limitations in the evaluations which are discussed in detail separately in chapter 5.

2.2 Flow and Boundary Conditions

For incompressible flows, the pressure gradient in the direction of flow is the most significant driving force. The simulations are carried out for a zero pressure gradient and adverse pressure gradient cases. Accurate control of the streamwise pressure gradient is essential to the study. In order to generate and maintain the required pressure gradient within

the flow field, the top wall of the domain is curved through the length of the domain. The curvature of the top wall is extracted from the DNS grid points and the top wall shape matches the geometry of the DNS. The curvature of the wall replicates the edge of the boundary layer along the length of the plate.

A ‘slip wall’ boundary condition is used at the top wall with zero shear stresses in the streamwise and normal directions. This is to ensure that the flow along the top wall surface is parallel to the streamlines in the freestream. Therefore, there is no flow crossing the top wall and the wall is located sufficiently far away and causes no disturbance to the freestream. A ‘no-slip wall’ boundary condition is applied at the plate surface. The boundary condition at the outlet is set to ‘outflow’. The outflow is a zero gradient condition for velocity and ensures that there is no back flow at the outlet of the domain.

A velocity inlet boundary conditions is applied to the domain inlet by specifying a mean inlet Blasius velocity profile at $Re_{\delta 0} = U_{fs}\delta_0 / v = 800$. The mean profiles of velocities (u, v) and turbulent structure properties (k and ε or ω) are also specified as boundary condition at the inlet to the domain and the inlet turbulence is based on the mean Reynolds stresses from the DNS mean statistics. The DNS employs an unsteady inlet using Orr-Somerfield and squire modes whereas the current study is at steady state. The steady state boundary conditions and the dimensionless inlet profiles employed, here as shown in Figure 2.2-Figure 2.4 were extracted from the mean flow statistics obtained from the DNS study [44].

The ε and ω values at the inlet and for all models, are estimated using the equations from the ANSYS FLUENT User’s Guide [45] as,

$$\varepsilon = \frac{0.09^{3/4} k^{3/2}}{0.4\delta_0}, \ \omega = \frac{0.09^{-1/4}\sqrt{k}}{0.4\delta_0} \tag{1}$$

While the Reynolds shear stresses are specified directly at the inlet for the RSM. The use of the inlet mean profiles from DNS in the current study is more accurate boundary conditions compared to those applied by Ghasemi et al.[18, 19] wherein the inlet boundary condition is specified with a constant turbulent intensity of 3% and a turbulent length scale equal to the boundary layer thickness. U_0 is freestream velocity equal to 1m/sec.

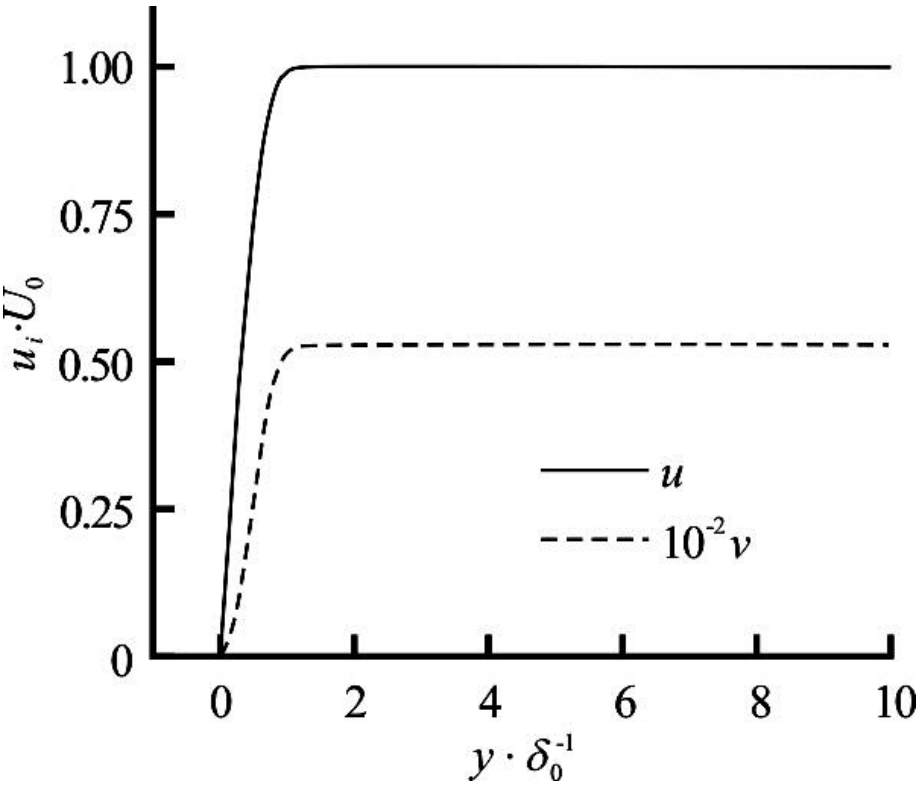

Figure 2.2 Mean velocity profile at inlet

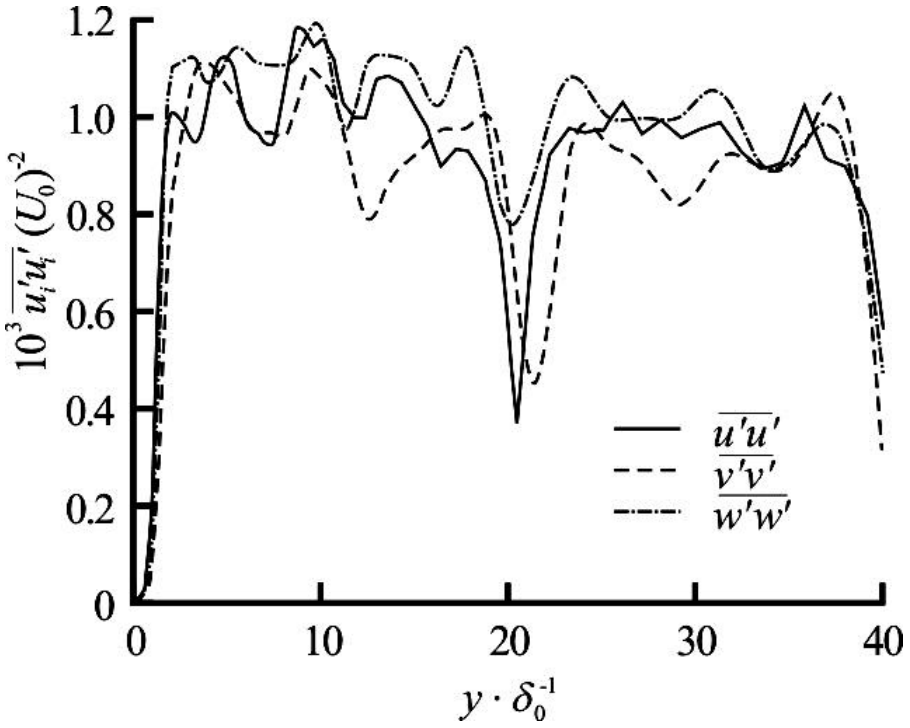

Figure 2.3 Reynolds normal stress profiles at inlet

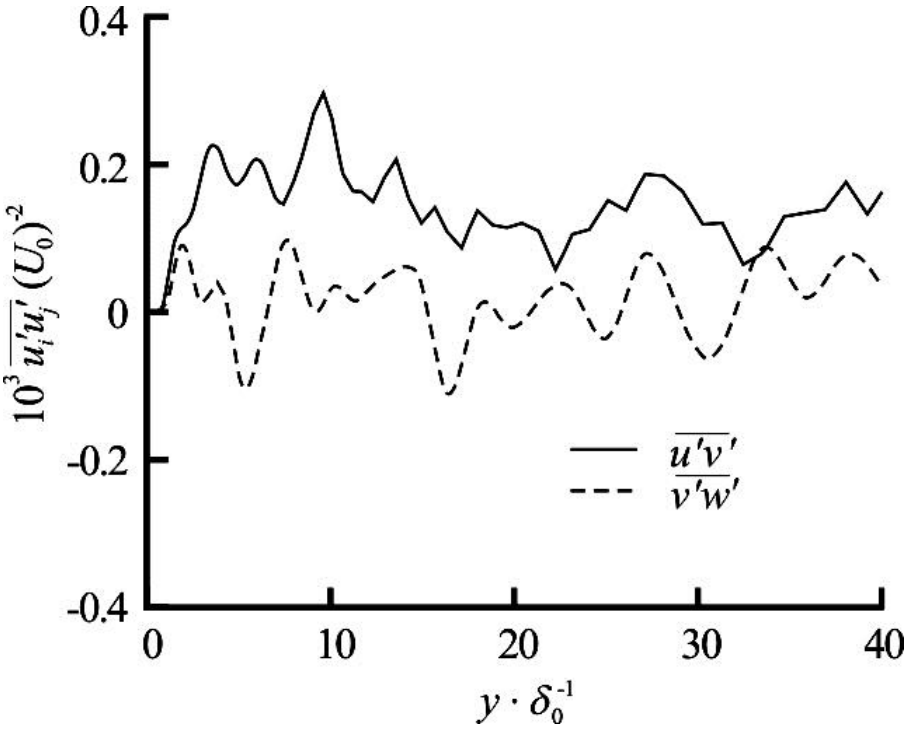

Figure 2.4 Reynolds shear stress profile at inlet

2.3 Simulation Table

A comprehensive overview of the different simulations performed in this study is contained in Table 2.1. The table shows a general outline for the models and settings used for the study. $(\beta \rightarrow streamwise \quad pressure \quad gradient \quad parameter)$

Table 2.1 Simulation design overview

Flow type	Viscous models	$L_x \times L_y \times L_z$ (m)	$n_x \times n_y \times n_z$	y^+
2D ZPG : $\beta = 0.0$	K-ε, SST K-ω, RSM, 4 equation K-ω SST	23.5×1.05×0	3 163×317×0	0.05
2D $\mathrm{APG}_{\mathrm{weak}}$: $\beta = -0.08$, 2D $\mathrm{APG}_{\mathrm{strong}}$: $\beta = -0.14$	K-ε, SST K-ω, RSM, 4 equation K-ω SST	15.7×1.05×0	3 163×317×0	0.05
3D ZPG (Fluent)	IDDES, LES (Dynamic stress kinetic energy transport model)	23.5×1.05×0.78	571x91x31 1441x97x51	< 1.0
3D ZPG (OpenFOAM)	LES (Dynamic Smagorinsky, Dynamic k-Eqn. Eddy viscosity model)	23.5x1.05x0.78	571x91x31 1441x97x51 2881x97x51	< 1.0

2.4 Solution Verification Methodology

Solution verification is important to estimate the numerical errors and grid uncertainties of a CFD simulation. Aspects of the simulation that cause numerical errors include: discretization, artificial dissipation, incomplete iterative and grid convergence, and computer round-off. To determine numerical errors generally involves performing a sensitivity study by varying the mesh spacing and/or time step size to a smaller value and evaluating the solution differences. The grids used and the results from the solution verification study for ZPG/APG simulations are discussed in detail here. The solution verification strategy and equations are as described in Xing [46, 47].

Here S_1, S_2, S_3 represent the fine, medium, and coarse grid solutions of any variable in the simulations, respectively. The relative percentage difference ($\delta\%$) between CFD results and correlation values, represented below as A, is calculated as,

$$\delta_{\%} = \left| \frac{A - S_1}{A} \right| \times 100\% \tag{2}$$

The solution verification method in place is the factor of safety method [46, 47] which requires the use of the following equations with the use of L2 norm for profiles [48],

$$\varepsilon_{21} = S_2 - S_1 \tag{3}$$

$$\varepsilon_{32} = S_3 - S_2 \tag{4}$$

$$\langle R_G \rangle = \frac{\|\varepsilon_{21}\|_2}{\|\varepsilon_{32}\|_2} \tag{5}$$

$$\langle p_G \rangle = \frac{\ln\left(\frac{\|\varepsilon_{32}\|_2}{\|\varepsilon_{21}\|_2} \right)}{\ln(r_G)} \tag{6}$$

Where r_G is the grid refinement ratio, $\Delta x_{G_2} / \Delta x_{G_1}$ and $\Delta x_{G_3} / \Delta x_{G_2}$, $\varepsilon_{\#\#}$ is the Change between $\hat{S}_{\#}$ for different grids, $S_{\#}$ is the value of a given variable with the grid refinement specified in the subscript.

Monotonic convergence is achieved when $0<(R_G)<1$. The ratio of the estimated order of accuracy to the theoretical order of accuracy of the numerical scheme is defined as,

$$P = \frac{\langle p_G \rangle}{p_{th}} \tag{7}$$

Where $\langle p_G \rangle$ is the profile averaged order of accuracy, p_{th} is the theoretical order of accuracy, $\langle R_G \rangle$ is the profile averaged convergence ratio.

The closer *P* is to 1 the closer the CFD simulation to the asymptotic range. The estimated error (δ_{RE}) and grid uncertainty (U_G) are defined as,

$$\delta_{RE} = \frac{\varepsilon_{21}}{r^{p_G} - 1} \tag{8}$$

$$U_G = [1.6P + 2.45(1-P)]\left|\delta_{RE}\right|,\ 0 < P \le 1 \tag{9}$$

$$U_G = [1.6P + 14.8(P-1)]\left|\delta_{RE}\right|,\ P > 1 \tag{10}$$

Where the grid uncertainty, U_G, is presented as a percentage of the correlation value or value from the fine grid solution at the same streamwise location. A lower magnitude of U_G usually indicates a better quality of CFD results.

Solution verification strategies for LES models have recently been proposed by Xing [49, 50]. However, in the current study, verification and validation for 3D LES models was not performed due to its high computational costs and lack of accurate results from 3D LES.

2.5 High Performance Computing

To ensure high fidelity simulations and more accurate results, a third-order MUSCL scheme is applied for the momentum and turbulence solvers in the solution methodology with a pressure-velocity coupled scheme. A convergence tolerance of 10^{-10} is set for all simulations to ensure that the iterative numerical errors are much smaller than the modeling grid errors such that the numerical errors could be neglected. These stringent scheme and high accuracy simulations can only be performed in a timely cost effective manner by employing available High Performance Computing resources. All simulations are performed using the commercial CFD software ANSYS Fluent v15.0 including RANS, LES and IDDES cases. Additionally, The LES simulations were also done using the open source software OpenFOAM v2.2.2. Chapter 5 provides more information on the capabilities and application of the open source software. All RANS, IDDES and LES cases were post processed using Scilab-5.4.1 and Tecplot360 2013. ANSYS Fluent simulations were performed on several local and network computing resources such as a local 8 and 16 core workstations with 8GB-32GB of RAM memory and the University of Idaho's network HPC resource – Big-STEM employing 12-16 CPU cores and over 32-64GB of RAM. All OpenFOAM software simulations are done on Linux cluster with UNIX / Shell scripting tools. A Virtual Box environment was setup on the local workstation to enable the use of Linux software on a Windows operating system workstation. High performance simulations were run on the Big-STEM Linux environment and the Idaho National Laboratory's HPC center which provides general use scientific computing capabilities to support efforts in advanced modeling and simulation. 'Fission' is an Appro distributed memory system with 12,512 processors, 25 TBytes of memory, and an aggregate peak processing rate of more than 90 Tflops.

Chapter 3: 2-Dimensional Zero Pressure Gradient

As previously described, the primary objective of the current study is to evaluate the ability of commercially used various RANS turbulence models to predict entropy generation and associated flow physics within a bypass transitional boundary layer flow.

3.1 Approach and Governing Equations

The Navier-Stokes equation is the fundamental governing equation for any given flow. However, solving the non-linear coupled Reynolds averaged N-S equations numerically is not trivial. This is due to the significance of the non-linear Reynold stress term in the N-S equation and the resulting well documented closure problem. Various turbulence models have been developed based on the Boussinesq eddy viscosity hypotheses [51] in order to effectively close the non-linear RANS equations. The hypothesis calculates the Reynolds stresses as,

$$\overline{u_i' u_j'} = \frac{2}{3} k \delta_{ij} - \nu_t \left(\frac{\partial \overline{u}_i}{\partial x_j} + \frac{\partial \overline{u}_j}{\partial x_i} \right) \tag{11}$$

The variable u_i is the velocity along the *x*, *y*, or *z* axis and u_j is the velocity along an axis different from the direction of u_i. This similarly applies to x_i as the location along a given axis *x*, *y*, or *z*. The turbulent viscosity is calculated differently depending on the model in use.

The transport equations for the different models can be summarized as,

$$\frac{\partial}{\partial t}(\rho k) + \frac{\partial}{\partial x_i}(\rho k u_i) = \frac{\partial}{\partial x_j}\left(\left(\mu + \frac{\mu_t}{\sigma_k} \right) \frac{\partial k}{\partial x_j} \right) + G_k - Y_k \tag{12}$$

$$\frac{\partial}{\partial t}(\rho [DV]) + \frac{\partial}{\partial x_i}(\rho [DV] u_i) = \frac{\partial}{\partial x_j}\left(\left(\mu + \frac{\mu_t}{\sigma_D} \right) \frac{\partial [DV]}{\partial x_j} \right) + G_D - Y_D + D_D \tag{13}$$

[*DV*] is the corresponding turbulence dissipation variable for the model.

3.1.1 k-epsilon Model

The formulations for the k-ε model are described in the ANSYS FLUENT Theory Guide [52].

The transport equations for the k-ε model require the following,

$$\begin{aligned}&[DV]=\varepsilon;\ G_k=-\rho\overline{u_i'u_j'}\frac{\partial u_j}{\partial x_i};\ Y_k=\rho\varepsilon;\ G_D=1.44\frac{\varepsilon}{k}G_k;\\&Y_D=1.92\rho\frac{\varepsilon^2}{k};\ D_D=0;\ \sigma_k=1.0;\ \sigma_D=1.3\end{aligned} \tag{14}$$

The turbulent viscosity is calculated as,

$$\mu_t=0.9\rho\frac{k^2}{\varepsilon} \tag{15}$$

3.1.2 k-omega SST Model

The formulations for the SST k-ω model are described in the ANSYS FLUENT Theory Guide [52].

The transport equations for the SST k-ω model require the following,

$$\begin{aligned}&[DV]=\omega, G_k=\min(-\rho\overline{u_i'u_j'}\frac{\partial u_j}{\partial x_i},10Y_k),\\&Y_k=0.09\rho k\omega, G_D=\frac{\alpha}{\nu_t}G_k, Y_D=\rho\beta\omega^2\\&\sigma_k=\frac{1}{F_1/1.176+(1-F_1)/1.0}\\&\sigma_D=\frac{1}{F_1/2.0+(1-F_1)/1.168}\end{aligned} \tag{16}$$

The turbulent viscosity is calculated as,

$$\mu_t=\frac{\rho k}{\omega}\frac{1}{\max\left(1,\frac{S_T F_2}{0.31\omega}\right)} \tag{17}$$

In these equations, not all the variables are constants as is the case for the k-ε model. The following lists the formulas for the variables within the transport and turbulent viscosity equations,

$$\alpha = 0.553F_1 + 0.440\left(1 - F_1\right) \tag{18}$$

$$\beta = 0.075F_1 + 0.0828\left(1 - F_1\right) \tag{19}$$

F_1 and F_2 are blending functions defined as,

$$\begin{aligned} F_1 &= \tanh\left(\Phi_1^4\right) \\ \Phi_1 &= \min\left[\max\left(\frac{\sqrt{k}}{0.09\omega y}, \frac{500\nu}{y^2\omega}\right), \frac{4\rho k}{1.168 D_\omega^+ y^2}\right] \\ D_\omega^+ &= \max\left[2\rho\frac{1}{1.168\omega}\frac{\partial k}{\partial x_j}\frac{\partial \omega}{\partial x_j}, 10^{-10}\right] \end{aligned} \tag{20}$$

$$\begin{aligned} F_2 &= \tanh\left(\Phi_2^2\right) \\ \Phi_2 &= \max\left[2\frac{\sqrt{k}}{0.09\omega y}, \frac{500\nu}{y^2\omega}\right] \end{aligned} \tag{21}$$

3.1.3 Reynold Stress Model

The formulations for the RSM are described in the ANSYS FLUENT Theory Guide [52].

The transport equation for the RSM is,

$$\begin{aligned} &\frac{\partial}{\partial t}\left(\rho\overline{u_i'u_j'}\right) + \frac{\partial}{\partial x_k}\left(\rho u_k \overline{u_i'u_j'}\right) = -\frac{\partial}{\partial x_k}\left(\rho\overline{u_i'u_j'u_k'} + \overline{p\left(\delta_{kj}u_i' + \delta_{ik}u_j'\right)}\right) \\ &+ \frac{\partial}{\partial x_k}\left(\mu\frac{\partial}{\partial x_k}\left(\overline{u_i'u_j'}\right)\right) - \rho\left(\overline{u_i'u_k'}\frac{\partial u_j}{\partial x_k} + \overline{u_j'u_k'}\frac{\partial u_i}{\partial x_k}\right) + \overline{p\left(\frac{\partial u_i'}{\partial x_j} + \frac{\partial u_j'}{\partial x_i}\right)} \\ &-2\mu\overline{\frac{\partial u_i'}{\partial x_k}\frac{\partial u_j'}{\partial x_k}} - 2\rho\Omega_k\left(\overline{u_j'u_m'}\varepsilon_{ikm} + \overline{u_i'u_m'}\varepsilon_{jkm}\right) \end{aligned} \tag{22}$$

ε_{ikm} and ε_{jkm} are permutation symbols.

3.1.4 Transitional 4-equation k-omega SST Model

The formulations for the transition SST model are described in the ANSYS FLUENT Theory Guide [52]. The transition SST model couples two additional transport equations with the SST k-ω transport equations. The first additional transport equation is for the intermittency and is defined as,

$$\frac{\partial}{\partial t}(\rho\gamma)+\frac{\partial}{\partial x_j}(\rho u_j\gamma)=\frac{\partial}{\partial x_j}\left(\left(\mu+\frac{\mu_t}{\sigma_\gamma}\right)\frac{\partial\gamma}{\partial x_j}\right)+P_{\gamma1}-E_{\gamma1}+P_{\gamma2}-E_{\gamma2} \tag{23}$$

The transition sources are defined as,

$$\begin{aligned} P_{\gamma1} &= 2F_{length}\rho S_T\left(\gamma F_{onset}\right)^{0.5} \\ E_{\gamma1} &= P_{\gamma1}\gamma \end{aligned} \tag{24}$$

F_{length} is an empirical correlation that controls the length of the transition region. The destruction/relaminarization sources are defined as,

$$\begin{aligned} P_{\gamma2} &= 0.06\rho\Omega\gamma F_{turb} \\ E_{\gamma2} &= 50\gamma P_{\gamma2} \end{aligned} \tag{25}$$

Ω is the vorticity magnitude. The onset of transition is controlled by,

$$Re_V=\frac{y^2S_T}{\mu},\ R_T=\frac{k}{\nu\omega} \tag{26}$$

$$\begin{aligned} F_{onset1} &= \frac{Re_V}{2.193Re_{\theta c}} \\ F_{onset2} &= \min\left(\max\left(F_{onset1},F_{onset1}^4\right),2.0\right) \\ F_{onset3} &= \max\left(1-\left(\frac{R_T}{2.5}\right)^3,0\right) \\ F_{onset} &= \max\left(F_{onset2}-F_{onset3},0\right) \\ F_{turb} &= e^{-\left(\frac{R_T}{4}\right)^4} \end{aligned} \tag{27}$$

$Re_{\theta c}$ is the critical Reynolds number where the intermittency first starts to increase in the boundary layer. The transport equation for the transition momentum thickness Reynolds number, $Re_{\theta t}$ is,

$$\frac{\partial}{\partial t}\left(\rho Re_{\theta t}\right)+\frac{\partial}{\partial x_j}\left(\rho u_j Re_{\theta t}\right)=\frac{\partial}{\partial x_j}\left(2\left(\mu+\mu_t\right)\frac{\partial Re_{\theta t}}{\partial x_j}\right)+P_{\theta t} \tag{28}$$

$$P_{\theta t}=0.03\frac{\rho^2U^2}{500\mu}\left(Re_{\theta p}-Re_{\theta t}\right)\left(1.0-F_{\theta t}\right) \tag{29}$$

$Re_{\theta p}$ is a proprietary empirical correlation for the transition onset and $F_{\theta t}$ is a function based on the boundary layer correlations calculated through FLUENT.

3.2 Analysis Method

The viscous dissipation for the mean velocity profile is the only contributor to entropy generation in laminar flow. Therefore, pointwise entropy generation rate equation applied for steady, two-dimensional, laminar boundary layer flows without significant fluctuations is,

$$TS'''\{y\}\approx\mu\left(\frac{\partial U}{\partial y}\right)^2 \tag{30}$$

However, the flow considered herein is unheated. Hence, the entropy generation occurs only due to the square of the gradients of the mean streamwise velocity. The integral over the boundary layer of the point- wise entropy generation rate provides the entropy generation rate per unit area,

$$TS''=\int_0^\delta S'''\mathrm{d}y \tag{31}$$

The dissipation coefficient, C_d, is a dimension- less variable that represents the entropy generation rate per unit area. The correlation by McEligot and Walsh estimate the dissipation coefficient multiplied by Re_θ as,

$$C_d Re_\theta = 0.1740 + 0.3315\lambda + 0.7881\lambda^2 \tag{32}$$

Both the displacement thickness and momentum thickness are integrated to δ in place of the upper in- definite bound. Fluctuations in bypass transitional flows necessitate additional terms to the entropy gene- ration equations used for laminar flow. These equations are outlined further by Walsh et al.[3]. The dimensionless entropy generation rate per unit area for a transitional flow is calculated as,

$$(S''\{\delta\})^+ \approx \int_0^\delta \left(\frac{\partial U^+}{\partial y^+}\right)^2 \mathrm{d}y^+ - \int_0^\delta (\overline{uv})^+ \left[\left(\frac{\partial U^+}{\partial y^+}\right)\right] \mathrm{d}y^+ -$$

$$\int_0^\delta [\overline{(u'^2)^+} - \overline{(v'^2)^+}] \frac{\partial U^+}{\partial x^+} \mathrm{d}y^+ -$$

$$\frac{\mathrm{d}}{\mathrm{d}x^+}\left[\int_0^\delta \frac{U^+}{2} \overline{(q^2)^+} \mathrm{d}y^+\right] \tag{33}$$

The variables in Eq.(33), are defined as,

$$(S'')^+ = \frac{TS''}{\rho u_\tau^3},\ (S''')^+ = \frac{T\nu S'''}{\rho u_\tau^4},\ U^+ = \frac{U}{u_\tau},\ u_\tau = \sqrt{\frac{\tau_w}{\rho}},$$

$$x^+ = \frac{x u_\tau}{\nu},\ y^+ = \frac{y u_\tau}{\nu},\ q^2 = u'^2 + v'^2 + w'^2 \tag{34}$$

u', v' and w' are the velocity fluctuations in the x, y and z directions, respectively.

The dimensionless form of Eq.(33) is the dissipation coefficient,

$$C_d = (S''\{\delta\})^{+}\left(\frac{C_f}{2}\right)^{3/2} \tag{35}$$

The skin-friction coefficient, C_f is calculated as,

$$C_f = \frac{\tau_w}{\rho U_{fs}^2\{x\}} \tag{36}$$

Intermittency is a measure for determining the laminar, transition, and turbulent regions of the flow and is calculated as,

$$\gamma = \frac{C_f - C_{f,\text{lam}}}{C_{f,\text{turb}} - C_{f,\text{lam}}} \tag{37}$$

The skin friction coefficient variables for the laminar and turbulent regions are calculated respectively as,

$$C_{f,\text{lam}} = \frac{0.664}{Re_x^{0.5}},$$

$$C_{f,\text{turb}} = \frac{0.455}{\ln^2(0.06Re_x)} \tag{38}$$

The intermittency is compared to transition length,

$$\eta_f = \frac{x - x_s}{x_e - x_s} \tag{39}$$

The x value for the beginning of transition, x_s, is when $\gamma = 0.005$ and the x value for the end of transition, x_g, is when $\gamma = 0.095$.

3.3 Solution Verification

The results from the solution verification study for the $k-\omega$ model are shown in Table 3.1. The three different mesh used were: Coarse (1581x159), Medium (2237x225) and Fine (3163x317) with ~250k, ~500k and ~1M grid points. The distance to the asymptotic range $(P_G = 1)$ is shorter for Re_θ than C_f.

Monotonic convergence is achieved. The grid uncertainty is below $1.6\%S_1$ for both variables. The solution verification study shows that the bypass transition results are independent of the grid resolution and thus all results are presented on the fine grid.

Table 3.1 Solution verification for bypass transitional boundary layer flow for ZPG

	Re_θ	C_f
R_G	0.6640	0.6135
P_G	1.1814	1.4097
P	0.5907	0.7049
$U_G\,(\%S_1)$	1.5082	0.0020

3.4 Results and Discussion

The bypass transition simulation results are compared with the DNS results from Nolan and Zaki [4, 8]. Additionally, the ZPG results are compared to the CFD results by Ghasemi et al. [18]. These comparisons and evaluations of results are shown in Figure 3.1to Figure 3.5 below.

The current simulations employ a more accurate inlet conditions and much finer mesh than the simulations by Ghasemi et al. The k, ω, ε profiles and Reynolds stress values are prescribed at the inlet, depending on the model in use, to match the conditions of the DNS simulation. Ghasemi et al. applied a velocity inlet boundary with a specified turbulence intensity of 3% and a turbulent length scale, where- as the mean velocity and turbulent structure profiles obtained from DNS data are specified at the inlet in the current study. Additionally, this study also examines both CFD predictions for entropy generation rates compared to that post-processed from DNS results.

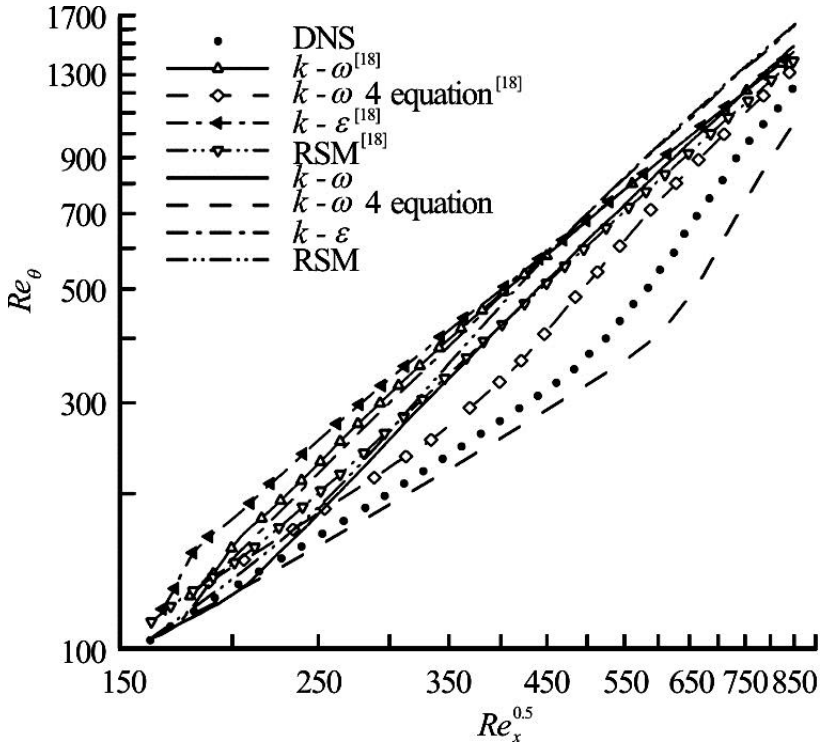

Figure 3.1 Re_θ versus $Re_x^{1/2}$

Figure 3.1 shows how Re_θ varies with $Re_x^{1/2}$. Figure 3.2 shows a more detailed view near the inlet region.

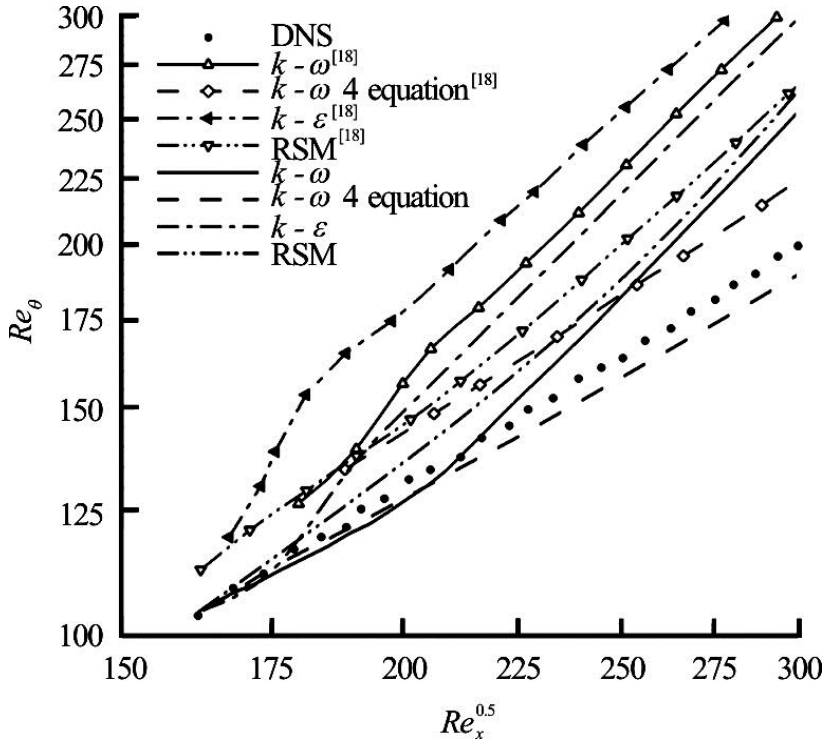

Figure 3.2 Re_θ versus $Re_x^{1/2}$ (detailed view near inlet)

The DNS data is linear in the log-log scale, the slope remains small up to $Re_x^{1/2} = 450$ and then the slope becomes much steeper indicating the onset of transition from laminar to turbulent boundary layer profile. The $k-\varepsilon$ model follows the DNS results near the inlet until $Re_x^{1/2} = 180$ where it transitions to turbulence. However, in that range results from Ghasemi et al.[18] show a steep slope and transition right at the inlet and much further away from DNS results. The RSM model shows similar trend like the $k-\varepsilon$ model but the results from Ghasemi et al. are further away from the DNS.

The $k-\omega$ model shows very close agreement to the DNS until $Re_x^{1/2} = 215$ and then deviates downstream whereas Ghasemi et al. [18] shows transition much earlier at $Re_x^{1/2} = 185$ and has a much larger difference in magnitude of Re_θ. The $k-\omega$ 4 equation

model results closely resemble the DNS results com- pared to all other simulations but the magnitude re- mains slightly lower than DNS data throughout the domain and the change in slope occurs at $Re_x^{1/2} = 575$ later than $Re_x^{1/2} = 475$ from DNS. The $k-\omega$ 4 equation model for Ghasemi et al. shows transition much earlier than DNS at $Re_x^{1/2} = 325$. The results in this study agree much better with the DNS results than the results from Ghasemi et al. in terms of overall magnitude of predicted Re_θ and the location of transition for all corresponding models.

Figure 3.3 and Figure 3.4 show how C_f and C_d vary with $Re_x^{1/2}$, respectively. The dissipation coefficient, C_d, provides a measure of the pointwise entropy generation rate, S''' (in non-dimensional form), within the boundary layer for ZPG case as described earlier. The DNS data has a linear slope in the turbulent regime. The laminar region is the initial downward slope, the rise indicates the transition region, and the small oscillations downstream are within the fully turbulent region. Figure 3.3 also shows the analytical laminar and turbulent lines. Similar to the trends seen in Figure 3.1, the $k-\varepsilon$ model and RSM model profile transition to turbulent very close to the inlet and remain turbulent throughout the flow field.

In Figure 3.3, the $k-\varepsilon$ model shows an initial laminar profile near the inlet, similar to DNS, before transition occurs downstream. The $k-\omega$ model shows a laminar region until $Re_x^{1/2} = 215$, where the onset of transition is predicted by the model. The $k-\omega$ model shows close agreement of predicted C_f to the DNS data from the inlet until the onset of transition and also in the turbulent region but transition occurs upstream compared to the $k-\omega$ 4 equation model and the DNS data. The $k-\omega$ 4 equation model shows better agreement with the DNS data for both C_d and C_f.

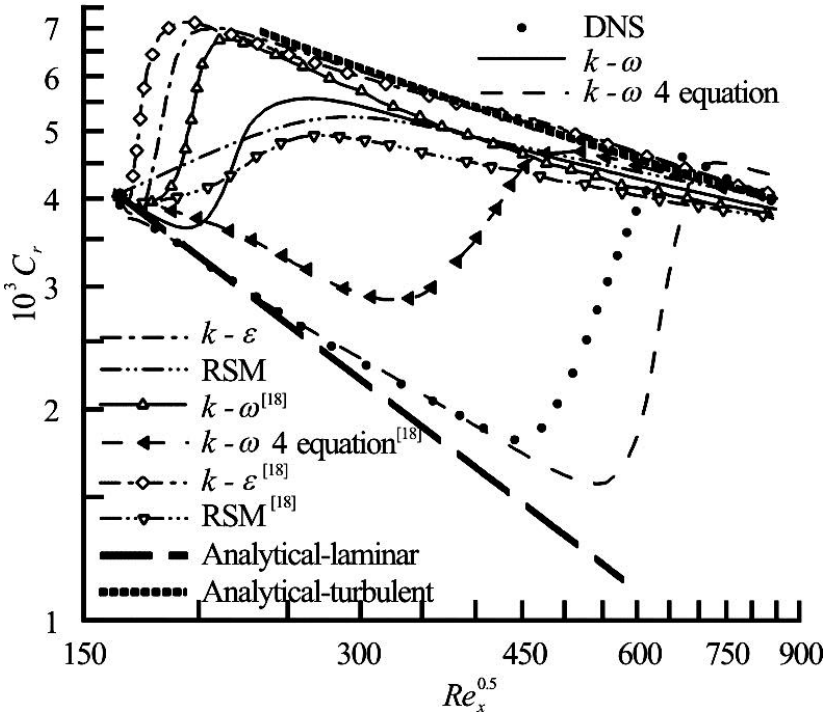

Figure 3.3 C_f versus $Re_x^{1/2}$

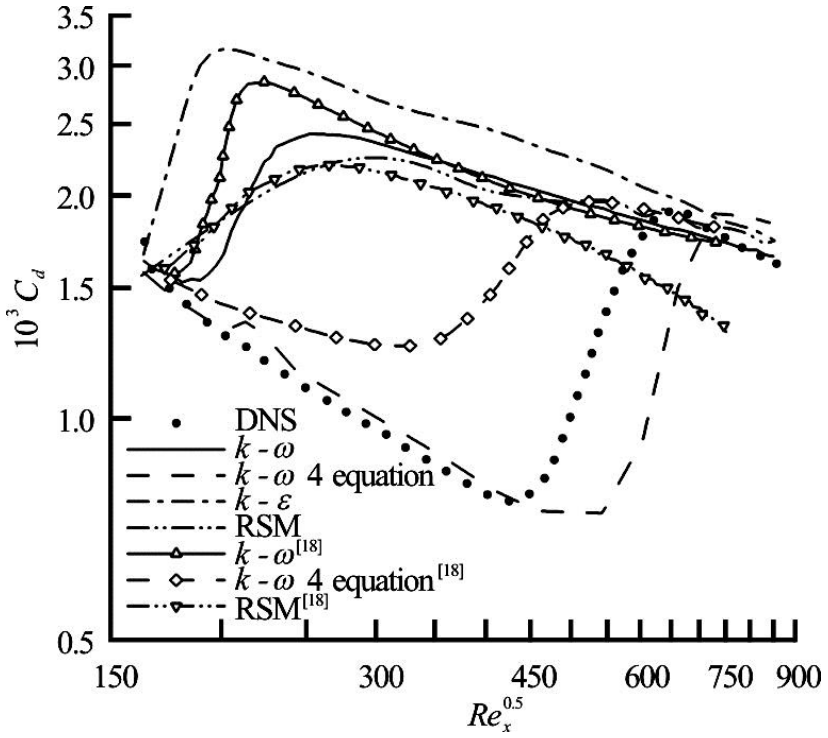

Figure 3.4 C_d versus $Re_x^{1/2}$

The analytical laminar and analytical turbulent lines shown in Figure 3.3 and Figure 3.4 are Blasius laminar profile and fully developed turbulent flow estimates from literature. The C_d and C_f predicted by the $k-\omega$ 4 equation model is very accurate compared to the DNS data until the transitional point in DNS at $Re_x^{1/2} = 450$. The model, however, over predicts the location of the onset of transition which occurs much later than DNS at $Re_x^{1/2} = 575$.

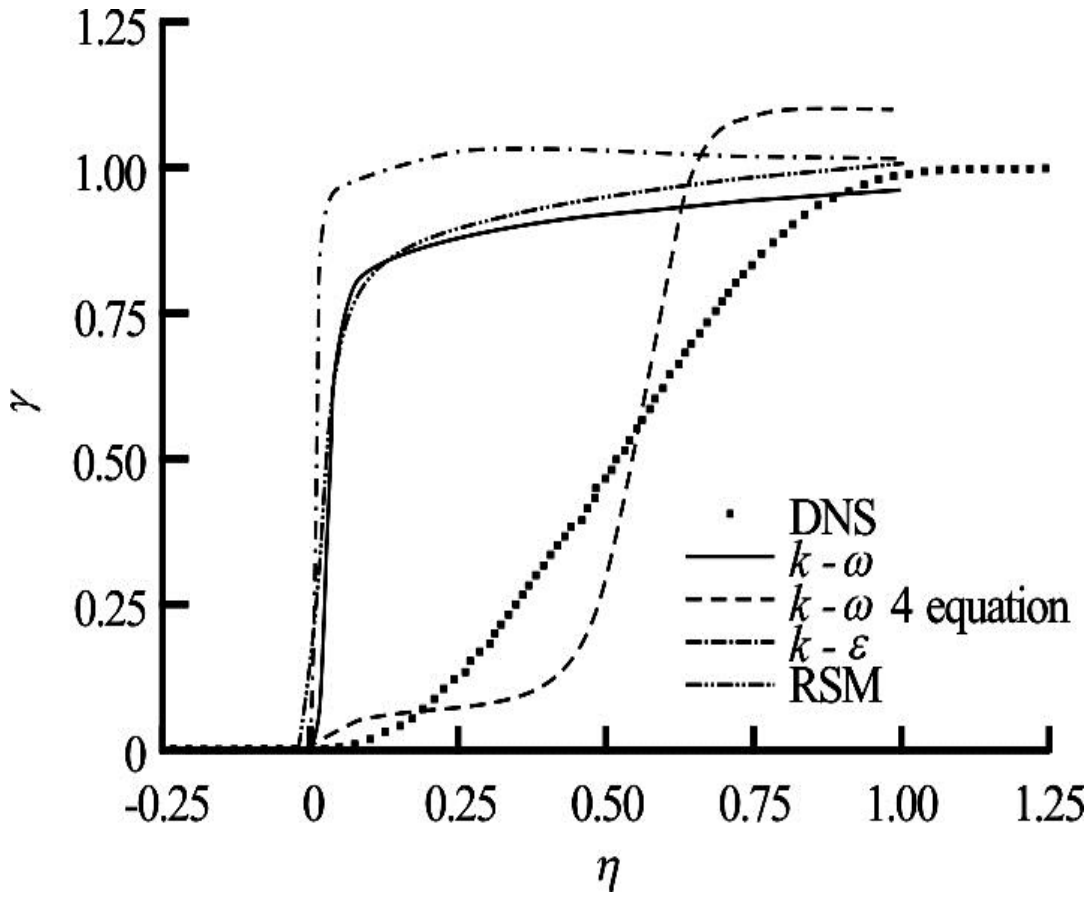

Figure 3.5 γ versus η

Figure 3.5 shows that all turbulence models examined in this study predict transition onset ($\gamma \leq 0.05$) earlier than the DNS data. γ is the intermittency and η is the similarity parameter in Blasius solutions. The $k\text{-}\omega$, $k\text{-}\varepsilon$, and RSM's demonstrate very similar trends with steeper slopes than the $k\text{-}\omega$ 4 equation models. The $k\text{-}\omega$ 4 equation model is the closest to the DNS data in predicting the transition onset location but over-predicts γ by as much as 10% in the fully turbulent region. All models tend to predict a much steeper slope in the transition region compared to the much smoother slope in the DNS data.

3.5 Conclusion

This chapter evaluates the capability of various RANS models to predict entropy generation rates in bypass transitional boundary layer flows under a zero pressure gradients case. The results show significant improvements over the RANS results by Ghasemi et al. [19] for all comparable models due to the employment of a much finer grid and more accurate inlet boundary conditions for velocity and turbulent structures.

Overall, the results from this chapter are more accurate and comparable to the DNS results than the results from Ghasemi with respect to trends and magnitude for all corresponding RANS models except for slight under prediction of magnitude within the fully turbulent regime.

The results suggest that the $k\text{-}\omega$ 4 equation model accurately predicts the boundary layer behavior and entropy generation for bypass transitional flows. All other models predict transition onset upstream of the location shown by the DNS data. However, the $k\text{-}\omega$ transition 4 equation model slightly over predicts the onset of transition from the DNS data based on the skin friction coefficient for the ZPG case.

Chapter 4: 2D Adverse Pressure Gradient

4.1 Approach and Analysis

The governing equations and analysis methodology used for the APG cases here is the same as in the case of ZPG case explained in the preceding chapter. The same four turbulence and transitional models: k-epsilon, k-omega SST, RSM and Transitional 4-equation k-omega SST are evaluated for the APG case.

Two different adverse pressure gradients are used for the analysis with $\beta = -0.08$ termed as APG_{Weak} and $\beta = -0.14$ termed as APG_{Strong}.

The strong and weak adverse pressure gradients are generated with the flowfield by employing varying curvature to the top slip wall boundary. The curvature and the overall domain size used in the study are directly extracted from the DNS study for accurate comparisons.

4.2 Solution Verification

Solution verification study for the APG cases were only done with the $k\text{-}\omega$ model. The results of the solution verification are very similar to that from the ZPG case and are tabulated in Table 4.1. The three different mesh used were: Coarse (1581x159), Medium (2237x225) and Fine (3163x317) with ~250k, ~500k and ~1M grid points.

Monotonic convergence is achieved and the grid uncertainty is below $1.20\%S_1$ for both variables. The solution verification study shows that the bypass transition results are independent of the grid resolution and thus all results are presented on the fine grid.

Table 4.1 Solution verification for bypass transitional boundary layer flow for APG

	Re_θ	C_f
R_G	0.6130	0.9937
P_G	1.4127	1.0184
P	0.7063	0.9203
$U_G\,(\%S_1)$	1.1478	0.0201

4.3 Results and Discussion

The bypass transition simulation results for APG cases are compared to the DNS results from Nolan and Zaki [4, 8] and the CFD results by Ghasemi et al. [19]. The APG results are evaluated using the skin- friction coefficient, C_f, and the approximate pointwise entropy generation rate, S'''.

4.3.1 APG$_{\text{Weak}}$: $\beta = -0.08$

Figure 4.1 shows comparison of C_f predicted from various models along the length of the flat plate versus $Re_x^{1/2}$ on a log-log scale for the weak APG case. In the DNS, C_f deviates from the analytical Blasius laminar approximation at about $Re_x^{1/2} = 200$ and is lower in the laminar region than the analytical approximation. The DNS predicts the onset of transition at about $Re_x^{1/2} = 400$ and fully developed turbulent flow beyond $Re_x^{1/2} = 550$. The analytical laminar and analytical turbulent lines shown in Figure 4.1 are Blasius laminar profile and fully developed turbulent flow estimates from literature.

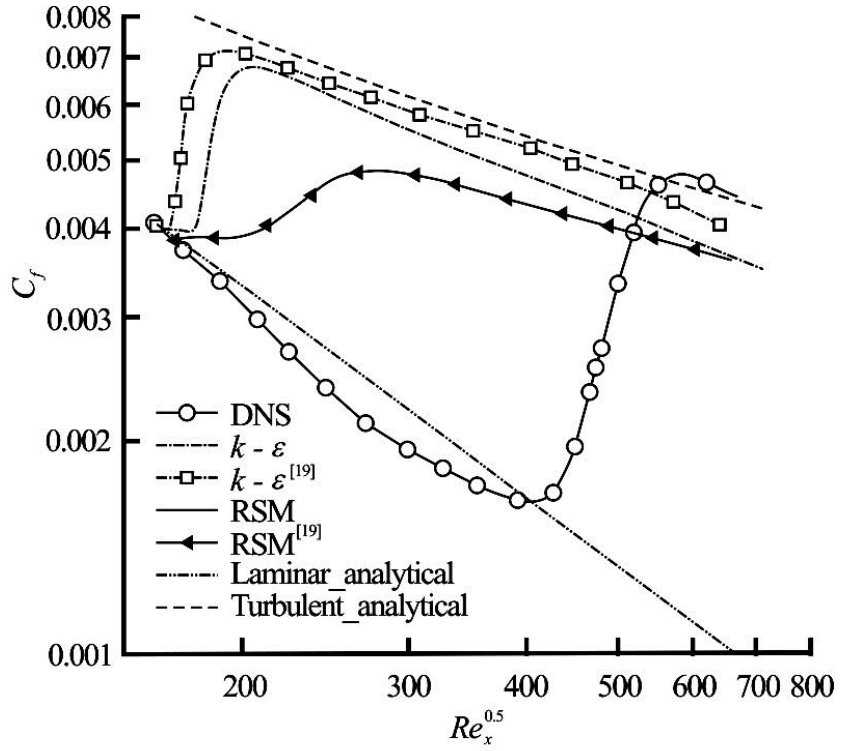

(a) k - ε and RSM model

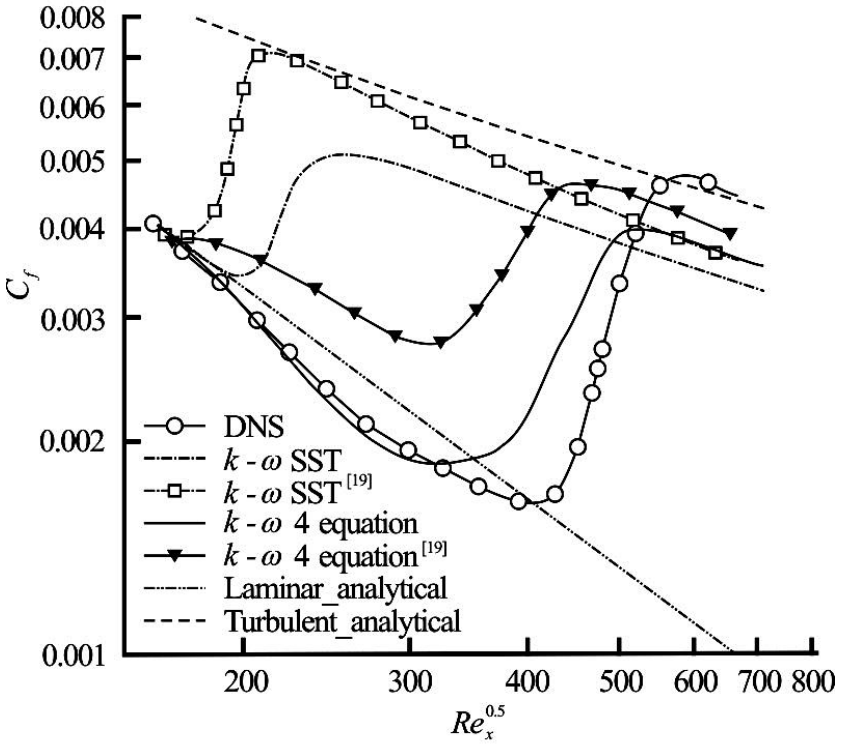

(b) k - ω SST and k - ω 4 equation model

Figure 4.1 C_f versus $Re_x^{1/2}$ for various RANS models for $\mathrm{APG}_{\mathrm{weak}}$

Figure 4.1(a) and Figure 4.1(b) shows $k-\varepsilon$, RSM, $k-\omega$ SST and transitional $k-\omega$ 4 Equation models compared with results from DNS and Ghasemi et al. [19] for the same models. The $k-\varepsilon$, RSM, $k-\omega$ SST and $k-\omega$ 4 equation models predict onset of transition at $Re_x^{1/2}$ = 170, 200, 220 and 350, respectively. All the above models compare better with DNS in predicting transition occurrence further downstream than by the corresponding models from Ghasemi et al. The transition $k-\omega$ 4 equation model predicts the flow very accurately and follows the DNS prediction very closely through the domain especially in the laminar and transition regimes. All four models in the present study under predict the skin-friction coefficient magnitude in the fully turbulent regime. Overall the results from this study are comparatively more accurate and in line with the DNS results than the results from Ghasemi et al. [19] in terms of trends and magnitude for all corresponding models especially, the transitional $k-\omega$ 4 equation model. The under prediction of C_f in the fully turbulent regime compared to Ghasemi et al. is due to the differences in the inlet boundary conditions specified. Specifying a constant turbulent intensity of 3% and a specific length scale rather a mean profile for turbulent structures as in the simulations by Ghasemi et al. could result in over prediction of fully turbulent regime compared to the actual capabilities of each RANS model. Figure 4.2 shows the comparison of approximate point-wise entropy generation rates, S''', as predicted by each model within the boundary layer plotted normal to the wall in terms of y^+. Since different models predict varying locations of transition, the entropy generation rate (S''') comparison is made at different locations along the flat plate for each model. These locations (indicated by $Re_x^{1/2}$ values) are selected at a point near the onset of transition as predicted by each model.

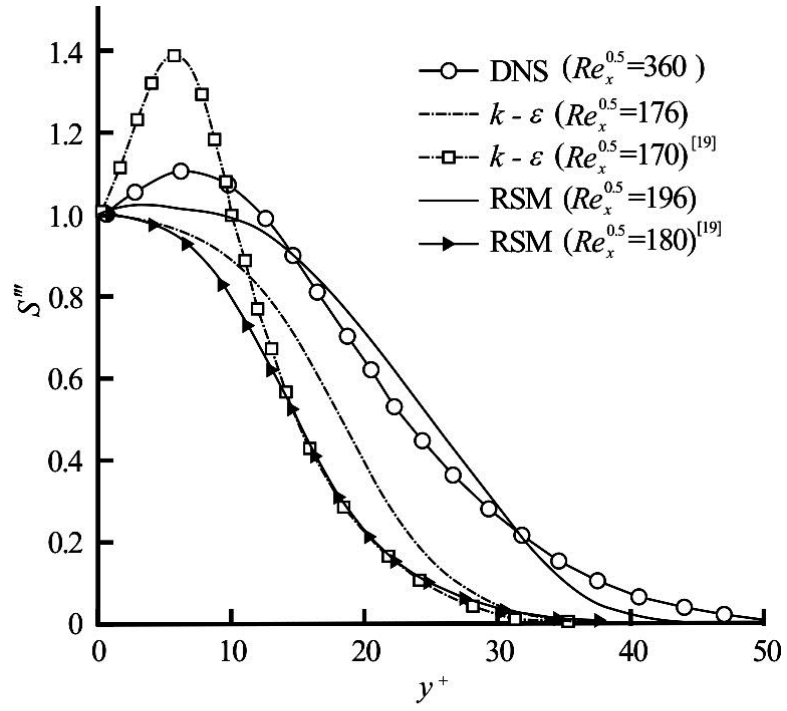

(a) k - ε and RSM model

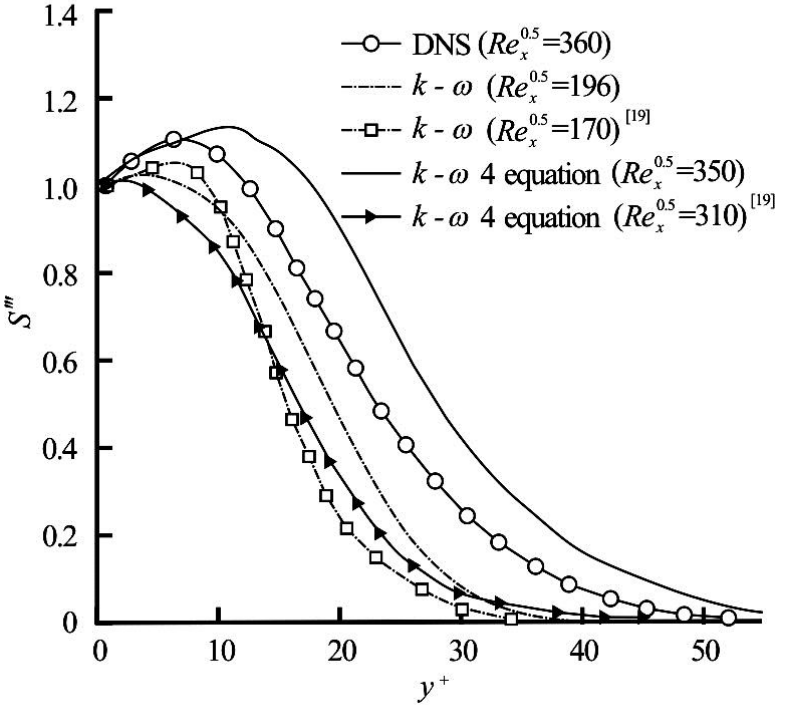

(b) k - ω SST and k - ω 4 equation model

Figure 4.2 S''' versus y^+ for various RANS models for $\mathrm{APG}_{\mathrm{weak}}$ near location of transition shown by values of $Re_x^{1/2}$

Figure 4.2(a) shows the $k-\varepsilon$ and RSM model and Figure 4.2(b) shows the $k-\omega$ SST and transitional $k-\omega$ 4 equation models compared with results from DNS [4] and Ghasemi. [19]. As seen from the figures the predictions from the current study are more accurate in terms of trends, magnitude and location than from Ghasemi for all corresponding models compared to DNS values. This is a direct result of better resolution within the boundary layer using more grid points near the wall and keeping $y^+ < 1$ at the first grid point away from the plate.

The predictions from the $k-\varepsilon$, RSM and $k-\omega$ SST are considerably closer to DNS values than Ghasemi et al. The transitional $k-\omega$ 4 equation model is the most accurate among all models although it slightly over-predicts the magnitude of S'''.

4.3.2 APG$_{\text{Strong}}$: $\beta = -0.14$

Figure 4.3 shows the comparison of C_f predicted from various models along the length of the flat plate versus $Re_x^{1/2}$ on a log-log scale. The analytical laminar and analytical turbulent lines shown in Figure 4.3 are Blasius laminar profile and fully developed turbulent flow estimates from literature. The DNS [4] results show that C_f deviates from the Blasius laminar approximation at approximately $Re_x^{1/2} = 180$ and predicts a lower C_f value in the laminar region as seen in the previous APG_{weak} case. The stronger adverse pressure gradient causes an earlier shift on predicted C_f from the analytical approximation. The DNS predicts the onset of transition at about $Re_x^{1/2} = 330$ and fully developed turbulent flow beyond $Re_x^{1/2} = 450$. The Stronger APG also shows an increase the maximum magnitude of S''' from 1.1 in the APG_{weak} case to a value of 1.5.

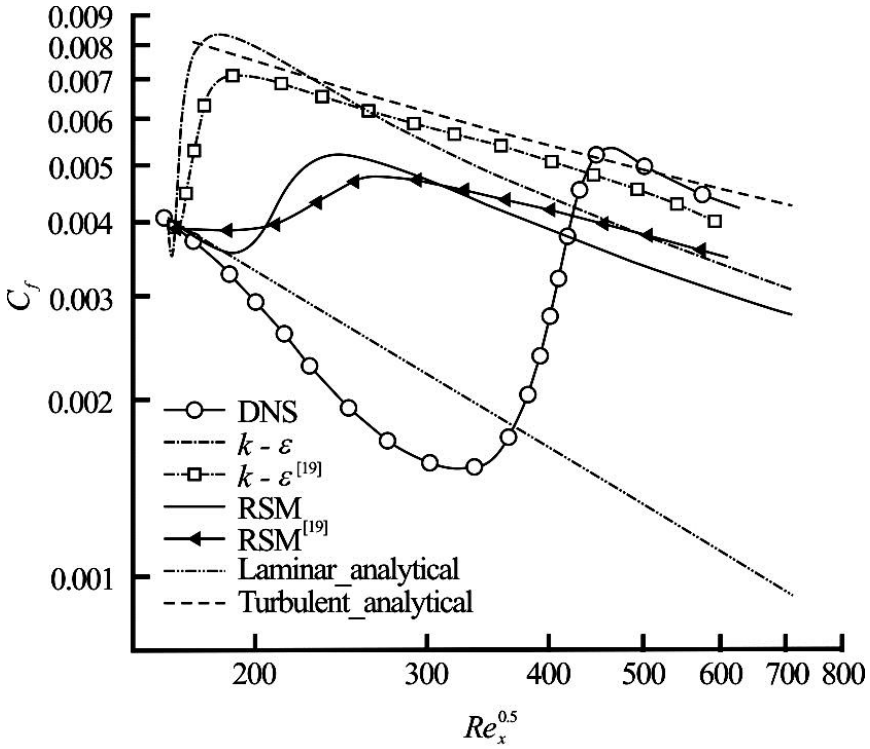

(a) k - ε and RSM model

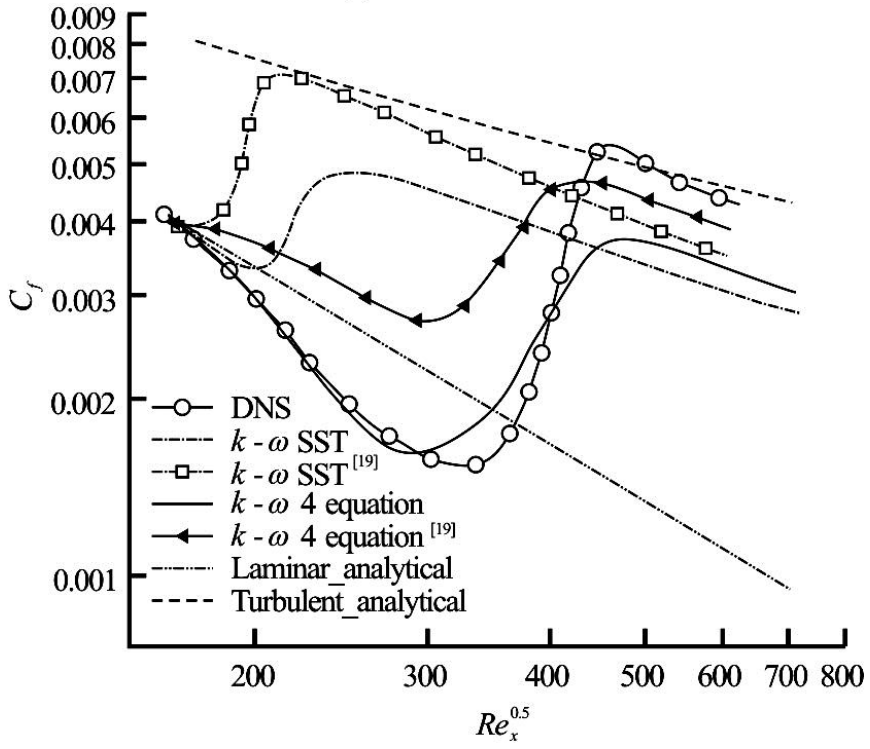

(b) k - ω SST and k - ω 4 equation model

Figure 4.3 C_f versus $Re_x^{1/2}$ for various RANS models $\mathrm{APG}_{\mathrm{Strong}}$

Figure 4.3(a) show the $k-\varepsilon$ and RSM model and Figure 4.3(b) shows the $k-\omega$ SST and transitional $k-\omega$ 4 equation models. The $k-\varepsilon$, RSM, $k-\omega$ SST and $k-\omega$ 4 equation models predict onset of transition at $Re_x^{1/2} = 170$, 195, 210 and 290, respectively.

The $k-\varepsilon$ model transitions to fully turbulent flow near the inlet for the current study as in the study by Ghasemi et al. This may be a result of the stronger pressure gradient being imposed on the flow and thereby indicating the models incapability in handling strong adverse pressure gradients effectively. The RSM, $k-\omega$ SST and $k-\omega$ 4 equation models follow similar trends as seen in the $\mathrm{APG}_{\mathrm{weak}}$ case with better comparison to DNS values than that by Ghasemi et al. [19].

Following the trend seen in previous results the models in current study under predict magnitude of C_f in the fully turbulent regime. Possible causes for such under prediction maybe as noted earlier in $\mathrm{APG}_{\mathrm{Weak}}$ results.

Figure 4.4 shows the comparisons of predicted approximate point-wise entropy generation rate S''' within the boundary layer normal to the wall near the location of transition point in terms of y^+.

It is noteworthy that, since the $k-\varepsilon$ model transitions near the inlet under the strong adverse pressure gradient, Figure 4.4(a) shows a turbulent profile of predicted entropy generation rate at $Re_x^{1/2} = 175$ for this model. The RSM, $k-\omega$ SST and $k-\omega$ 4 equation models predict more accurate comparable profiles for S''' near their transition location than the models by Ghasemi et al. [19]

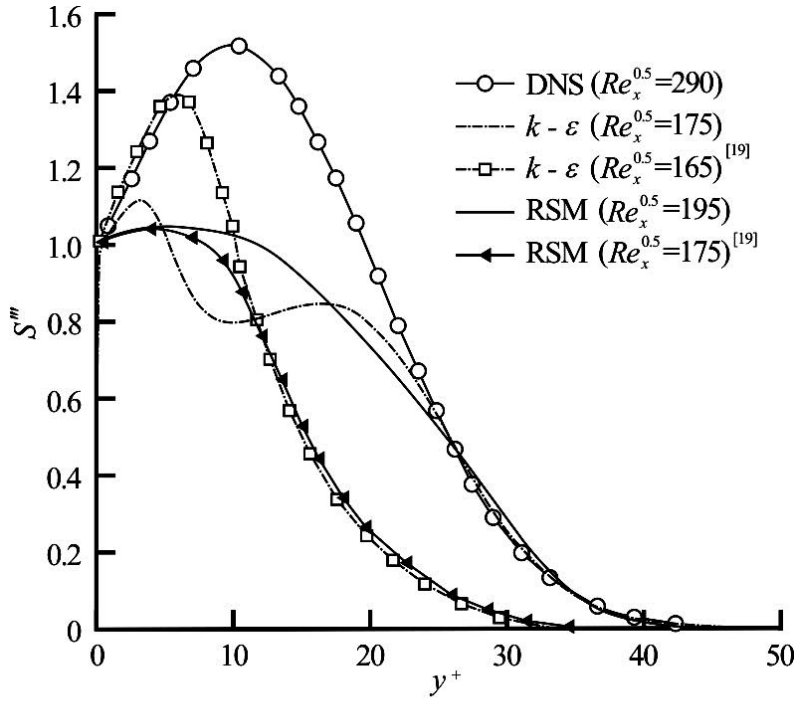

(a) k - ε and RSM model

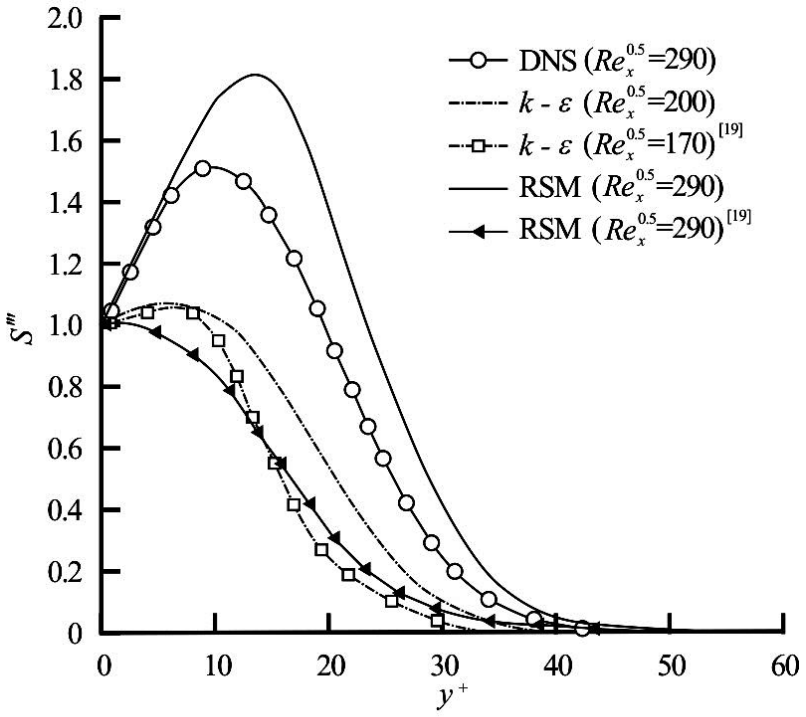

(b) k - ω SST and k - ω 4 equation model

Figure 4.4 S''' versus y^+ for various RANS models $\mathrm{APG}_{\mathrm{Strong}}$ near location of transition shown by values of $Re_x^{1/2}$

4.4 Conclusion

Overall, the results from this chapter are more accurate and comparable to the DNS [4] results than the results from Ghasemi [19] for both APG_{weak} and APG_{strong} cases with respect to trends and magnitude for all corresponding RANS models except for slight under prediction of magnitude within the fully turbulent regime. APG_{strong} has a higher maximum value of S''' in the boundary layer than APG_{weak} case indicating a direct relationship between the pressure gradient and entropy generation rates.

The results suggest that the $k-\omega$ 4 equation model accurately predicts the boundary layer behavior and entropy generation for bypass transitional flows. All other models predict transition onset upstream of the location shown by the DNS data. How- ever, the $k-\omega$ transition 4 equation model slightly under predicts the onset of transition from the DNS data based on the skin friction coefficient for the APG cases.

Chapter 5: Bypass 3D Zero Pressure Gradient using LES and IDDES

5.1 Introduction

The RANS models described in the previous chapters are robust and computationally inexpensive. However, these models fail to resolve the turbulence scales and physics. RANS only resolves the mean flow quantities. In RANS, the instantaneous velocity flied is decomposed to be time averaged quantities and all of the instantaneous turbulence structures are modeled. This leads to high levels of dissipation of the turbulent kinetic energy within the flow being simulated.

Progressively, new methodologies like Detached Eddy Simulations (DES), Delayed Detached Eddy Simulation (DDES), Improved Delayed Detached Eddy Simulation (IDDES) and Large Eddy Simulations have been developed to resolve the majority of turbulence scales and reduce the modelled parameters to the sub-grid scale levels. These methods, especially LES and IDDES, are considerably better in comparison to RANS for prediction of turbulence structures within the flow being simulated. However, each has its own limitation, viz., LES is computationally more expensive and is not easily setup to simulate wall bounded flows.

Large eddy simulation (LES) is a popular technique for simulating turbulent flows. Turbulent flows are characterized by eddies with a wide range of length and time scales. The largest eddies are typically comparable in size to the characteristic length of the mean flow. The smallest scales are responsible for the dissipation of turbulent kinetic energy. An implication of Kolmogorov's (1941) theory of self-similarity is that the large eddies of the flow are dependent on the geometry while the smaller scales more universal [53]. This feature allows one to explicitly solve for the large eddies in a calculation and implicitly account for the small eddies by using a subgrid-scale model (SGS model).

In LES, large eddies are directly computed (resolved), while small eddies are modelled as shown below in Figure 5.1. The ‘(k)’ is the turbulent kinetic energy and ‘E (k)’ is the corresponding ‘energy spectrum function.’ The distribution shown is typical energy spectrum within a turbulent flow.

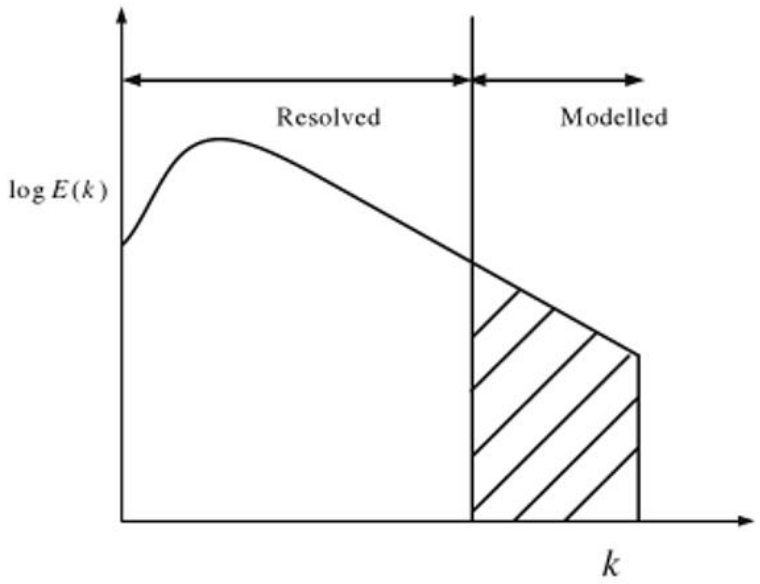

Figure 5.1 A typical energy spectrum captured by LES (Dewan [54])

Mathematically, one may think of separating the velocity field into a resolved and sub-grid part. The resolved part of the field represent the "large" eddies, while the subgrid part of the velocity represent the "small scales" whose effect on the resolved field is included through the subgrid-scale model. Momentum, mass, energy and other passive scalars are transported mostly by large eddies. Large eddies are problem dependent, i.e., they are dictated by the geometries and boundary conditions of the flow being considered. Small eddies are less dependent on the geometry, tend to be isotropic and are consequently universal compared to large eddies. Resolving only the large eddies allows for use of coarser mesh sizes and large time steps in LES than in DNS.

LES still requires substantially finer meshes than those typically used for RANS calculations. LES thus falls between DNS and RANS in terms of computational cost. LES has to be run for a sufficiently long flow time to obtain stable statistics of the flow being simulated. The computational cost involved with LES is normally orders of magnitudes higher than that from steady RANS calculations in terms of memory and CPU time [53, 54]. Therefore, high performance computing (parallel computing) is a necessity for LES.

The Improved Delayed Detached Eddy Simulation (IDDES) model [55] is a hybrid RANS-LES model (consisting of a combination of various new and existing techniques) that provides a more flexible and convenient scale-resolving simulation (SRS) model for high Reynolds number flows. Since the model formulation is relatively complex and the application of the model is non-trivial, it is recommended that you consult the original publications of Shur et al. [55].

The IDDES model has the following goals in addition to the formulation of the standard DES model: to provide shielding against Grid Induced Separation (GIS), similar to the DDES model [56] and to allow the model to run in Wall Modeled LES (WMLES) mode in case unsteady inlet conditions are provided to simulate wall boundary layers in unsteady mode. The IDDES model is designed to allow the LES simulation of wall boundary layers at much higher Reynolds numbers than standard LES models.

The IDDES model implemented in ANSYS FLUENT is based on the SST model [57] with the application of IDDES modifications as given in [55]. Similar to DES, the k-equation of the SST model is modified to include information on the local grid spacing. In case the grid resolution is sufficiently fine, the model will switch to LES mode. However, the goal is to cover stable boundary layers (meaning no unsteady inlet conditions and no upstream obstacles

generating unsteadiness) in RANS mode. In order to avoid affecting the SST model under such conditions, the IDDES function provides shielding similar to the DDES model, meaning it attempts to keep the boundary layer in steady RANS mode even under grid refinement.

In order to resolve the wall boundary layer in WMLES mode, unsteady inlet conditions need to be provided by employing either the *Vortex Method* or *Spectral Synthesizer*. The model can also be run with the Embedded LES (ELES) option and the IDDES option in ANSYS FLUENT.

For the present study, IDDES model was run only using ANSYS Fluent. Dynamic LES models were run using both FLUENT and OpenFOAM.

5.1.1 CFD OpenFOAM (v2.2.2)

CFD OpenFOAM is a free, open source commercial CFD software package managed and distributed by ESI – OpenCFD group [58]. OpenFOAM has an extensive range of features to solve anything from complex fluid flows involving chemical reactions, turbulence and heat transfer, to solid dynamics and electromagnetics. It includes tools for meshing, notably snappyHexMesh, a parallelized mesher for complex CAD geometries, and for pre- and post-processing. Almost everything (including meshing, and pre- and post-processing) runs in parallel as standard, enabling users to take full advantage of computer hardware at their disposal.

By being open, OpenFOAM offers users complete freedom to customize and extend its existing functionality, either by themselves or by others. It follows a highly modular code design in which collections of functionality (e.g. numerical methods, meshing, physical models, etc.) are each compiled into their own shared library. Executable applications are then created that are simply linked to the library functionality. OpenFOAM includes over 80 solver

applications that simulate specific problems in engineering mechanics and over 170 utility applications that perform pre- and post-processing tasks, e.g. meshing, data visualization, etc.

OpenFOAM offers complete freedom to customize and extend its current functionality (C++ programming) for application in flow being considered. In terms of use for LES modeling, it has 24 LES Turbulence models and incorporates 7 different LES delta's and filters combination depending on the application [59]. The growing large user base, both academic and commercial, provides extensive support through online forums and the OpenFOAM web releases and updates.

OpenFOAM is advantageous in terms of: friendly syntax for partial differential equations, unstructured polyhedral grid capabilities, automatic parallelization of applications written using OpenFOAM high-level syntax, wide range of applications and models ready to use, commercial support and training provided by the developers, and no license costs. However, it does have some disadvantages in terms of: absence of an integrated graphical user interface, and the programmer's guide [60] does not provide sufficient details, making the learning curve very steep if you need to write new applications or add functionality.

5.2 Governing Equations for Large Eddy Simulation

Calculation of the Courant-Friedrichs-Lewy (CFL) number is made by the equation below where C is the CFL number, Δt is the time step size, u is the velocity in the streamwise direction, and Δx is the step size in the streamwise direction.

$$C = \frac{u\Delta t}{\Delta x} \tag{40}$$

As detailed earlier, LES requires modelling of the part of the inertial sub range and into the beginning of the dissipation scales. LES resolves the large flow structures by selecting

appropriate filter function. The short wave information, lost through filtering, is called the subgrid component. The modelling of small scale unresolved stresses is done using a subgrid scale model (SGS model). The filtered Navier-Stokes equation can be written in the tensor notation for instantaneous, three-dimensional flow as,

$$\frac{\partial}{\partial t}\left(\bar{u}_i\right)+\frac{\partial}{\partial x_j}\left(\bar{u}_i\bar{u}_j\right)=-\frac{\partial \bar{p}}{\partial x_i}+\nu\frac{\partial}{\partial x_j}\left(\frac{\partial \bar{u}_i}{\partial x_j}+\frac{\partial \bar{u}_j}{\partial x_i}\right)-\frac{\partial \tau_{ij}}{\partial x_j} \tag{41}$$

The filtered thermal energy equation (without considering the source term) is,

$$\frac{\partial \bar{\theta}}{\partial t}+\bar{u}_j\frac{\partial \bar{\theta}}{\partial x_j}=-\frac{\partial q_i}{\partial x_i} \tag{42}$$

Here τ_{ij} denotes the SGS stress tensor and is defined as

$$\tau_{ij}=\left(\overline{u_i u_j}\right)-\left(\bar{u}_i\bar{u}_j\right) \tag{43}$$

Likewise the SGS heat flux tensor in the thermal energy equation is defined as

$$q_i=\left(\overline{u_i\theta}\right)-\left(\bar{u}_i\bar{\theta}\right) \tag{44}$$

The SGS stress term contains unknown velocity correlation which has to be modeled. This tensor describes the interaction between the large resolved grid scales and the small unresolved SGS.

5.2.1 LES Filtering

The difference between the LES model and DNS is filtering. Filtering occurs inside the given SGS model. The variation of the SGS model can be categorized into either implicit or explicit formulations of the NS equations.

For implicit filtering, LES resolves length scales based on the size of the grid spacing. For explicit filtering, one can specify the filter width. The implicit LES modeling relies on

the numerical errors of the particular spatial and temporal discretization schemes. The explicit LES modeling separates the numerical and modeling errors by changing the filter width and the grid size. Some models are considered to have both implicit and explicit filtering. One such model is the dynamic model developed by Germano et al. [61] which applies an explicit filtering step to compute the SGS stress tensor to the Smagorinsky SGS model.

5.2.2 Wall Modelling in LES / IDDES

In a wall bounded flow, the smallest scales are much smaller in the vicinity of a solid wall than those far away. Therefore, in such a situation it is possible to solve for a significant fraction of the energy away from the wall with a reasonably fine mesh, whereas in the vicinity of a solid wall some suitable turbulence model needs to be used as its accurate resolution requires an extremely fine mesh close to the wall. Several models have been proposed in the literature for the treatment of the wall. Two approaches commonly used to treat solid walls in LES are: Models based on equilibrium laws (i.e., logarithmic law) and The two layer models employing RANS equations to estimate wall shear stress (like proposed by Balaras et al. [62])

5.3 LES and IDDES Models

Several models for the subgrid scales exists in literature. The use of each SGS model is dependent on the application to the flow being considered. Broadly, the LES SGS models can be classified into three groups [63]: Smagorinsky SGS models, Dynamic SGS models and the Scale Similarity SGS models. Subgrid scale models such as the Smagorinsky (1963) [64] cannot be used for spatially growing simulation of the transition to turbulence of flat pate boundary layer, unless large amplitude perturbations are introduced at the upstream boundary: they are over-dissipative, and the flow remains laminar [65]. The present study used only the following SGS and IDDES models for the 3D ZPG flow problem.

5.3.1 Dynamic Smagorinsky-Lilly SGS Model

The sub-grid scale eddy viscosity for the Smagorinsky model is,

$$\mu_t = \rho L_s^2 \left|S_T\right| \tag{45}$$

L_s is the mixing length for the SGS and is defined in FLUENT as,

$$L_s = \min\left(0.41y, C_s V^{1/3}\right) \tag{46}$$

V is the volume of the computational cell and C_s is the Smagorinsky constant.

The dynamic Smagorinsky-Lilly model replaces the constant C_s with the following equations,

$$\begin{aligned} L_{ij} &= \left(\rho\overline{u_i' u_j'}\right) - \frac{1}{\rho}\left(\overline{\rho u_i'}\,\overline{\rho u_j'}\right) \\ M_{ij} &= -2\left(\left(2\Delta\right)^2 \rho S_T S_{ij} - \Delta^2 \rho S_T S_{ij}\right) \\ C_s^2 &= \frac{\left(L_{ij} - L_{kk}\delta_{ij}/3\right)}{M_{ij}M_{ij}} \end{aligned} \tag{47}$$

Δ is the grid filter width. The SGS turbulent stresses are computed as,

$$\tau_{ij} - \frac{1}{3}\tau_{kk}\delta_{ij} = -\rho\nu_t\left(\frac{\partial u_i}{\partial x_j} + \frac{\partial u_j}{\partial x_i}\right) \tag{48}$$

5.3.2 Dynamic Kinetic Energy 1-equation Eddy-Viscosity SGS Model

The subgrid-scale turbulence can be better modeled by accounting for the transport of the subgrid-scale turbulence kinetic energy. The dynamic subgrid-scale kinetic energy model in ANSYS Fluent replicates the model proposed by Kim and Menon [66]. The subgrid-scale kinetic energy, which is obtained by contracting the subgrid-scale stress, is defined as

$$k_{sgs} = \frac{1}{2}\left(\overline{u_k^2} - \bar{u}_k^2\right) \tag{49}$$

The subgrid-scale eddy viscosity, μ_t, is computed using, k_{sgs} as

$$\mu_t = C_k \rho k_{sgs}^2 \Delta f \tag{50}$$

Δf is the filter-size computed from $\Delta f = V^{1/3}$. The subgrid-scale stress can then be written as

$$\tau_{ij} - \frac{2}{3}\rho k_{sgs}\delta_{ij} = -2C_k \rho k_{sgs}^2 \Delta f \overline{S_{ij}} \tag{51}$$

k_{sgs} is obtained by solving its transport equation,

$$\rho \frac{\partial k_{sgs}}{\partial t} + \rho \frac{\partial \overline{u_j}\,\overline{k}_{sgs}}{\partial x_j} = -\tau_{ij}\frac{\partial \overline{u_i}}{\partial x_j} - C_\varepsilon \rho \frac{k_{sgs}^{3/2}}{\Delta f} + \frac{\partial}{\partial x_j}\left(\frac{\mu_t}{\sigma_k}\frac{\partial k_{sgs}}{\partial x_j}\right) \tag{52}$$

In the above equations, the model constants, C_k and C_ε are determined dynamically [66]. σ_k is hardwired to 1.0.

5.3.3 Improved Delayed Detached Eddy Simulation (IDDES) Model

IDDES models treat the near wall region in a RANS-like manner and the rest of the flow in an LES-like manner [67]. This approach avoids the need for a DNS grid resolution in the near wall region like LES models require. The IDDES model is based on the SST model in the near wall region and the LES model in the free-stream region. Modifications are made to the SST model in the form of an additional sink term in the TKE transport,

$$\frac{\partial}{\partial t}(\rho k) + \frac{\partial}{\partial x_i}(\rho k u_i) = \frac{\partial}{\partial x_j}\left(\left(\mu + \frac{\mu_t}{\sigma_k}\right)\frac{\partial k}{\partial x_j}\right) + G_k - Y_k - \frac{\rho\sqrt{k^3}}{l_{IDDES}} \tag{53}$$

l_{IDDES} is a length scale based on the RANS turbulent length scale and the LES grid length scale. The equation for the length scale is complicated and will only be briefly discussed here. The general DDES formulation from Spalart et al. [56] is,

$$l_{DDES} = l_{RANS} - \left(1 - \tanh\left[\left(8r_d\right)^3\right]\right)\max\left\{0, \left(l_{RANS} - l_{LES}\right)\right\} \tag{54}$$

5.4 Simulation Setup and Analysis Method

The grid used for the zero pressure gradient 2D RANS simulation was extruded in the spanwise direction (z = 0.78m) to create the 3D geometry and grid for the LES and IDDES simulation using pointwise v17.0R2. A few different meshes were created to check grid sensitivity effects for the simulation. The initial 3D IDDES grid created was as the same used in his thesis by Owen [68] with a grid distribution of 571x91x31 (~1.6M grid points) in the streamwise (*x*), normal (*y*) and the spanwise (*z*) directions (coordinates). The grid was further systematically refined in all directions to produce finer grid of ~6.9M grid points with a distribution of *1441x97x51* in the x, y and z directions. Another finer mesh was created by doubling the number of points in the streamwise direction to produce a ~13.8M grid set.

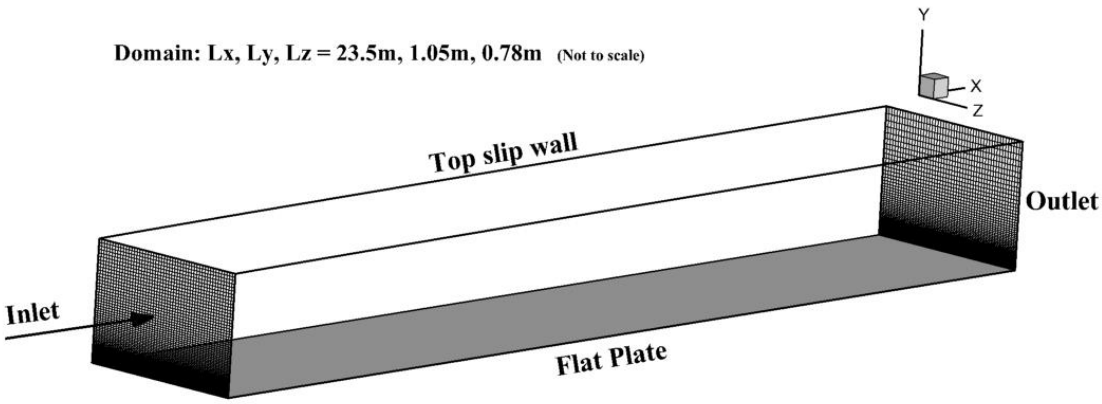

Figure 5.2 3D Domain used for LES and IDDES simulation

(Grid shown on inlet and outlet faces)

The inlet and outlet boundary conditions are similar to the boundaries for the RANS models. The profiles of mean velocity in the stream wise, normal and spanwise directions, the mean turbulence kinetic energy, dissipation rate and the mean Reynolds stresses were specified at the inlet of the domain. The instantaneous fluctuations for the inlet profiles were introduced artificially at each time step within ANSYS FLUENT.

The Spectral Synthesizer / Vortex Method hardcoded within FLUENT creates the inlet perturbations with profiles of the variables u, v, w, k, ε,$\overline{u'u'}$, $\overline{v'v'}$, $\overline{w'w'}$, $\overline{u'v'}$, $\overline{v'w'}$, and $\overline{u'w'}$ specified at the inlet. The left and right span-wise boundary conditions are zero gradient. A second-order, implicit transient solver, central difference momentum solver, and second-order pressure solver are implemented. The SIMPLE scheme is implemented for the pressure-velocity coupling. The convergence tolerance within each time step is 1×10^{-5}. The integral of the skin friction coefficient across the plate surface is monitored to determine statistical steadiness. Once the flow is statistically steady, the flow statistics are sampled over time for post-processing.

LES and IDDES models require both three-dimensional and unsteady simulations, necessitating different post-processing methodologies. The total TKE from the models under investigation consists of the resolved and modeled TKE [69]. This topic is investigated further in Xing et al. 2012 [70]. The resolved TKE is evaluated using the resolved velocity fluctuations. Reynolds decomposition dictates that the instantaneous velocity component is split into the mean and fluctuating components.

$$u_i\{x,y,z,t\} = \bar{u}_i\{x,y,z\} + u_i'\{x,y,z,t\} \tag{55}$$

The instantaneous and mean velocity components are calculated by FLUENT. The time-averaged velocity component is evaluated as,

$$\bar{u}_i\{x,y,z,t\} = \frac{1}{T_0}\int_t^{t+T_0} u\{x,y,z,t\}\,dt \tag{56}$$

T_0 is the averaging time. The resolved Reynolds stresses are calculated as,

$$\overline{u_i'u_j'} = \frac{1}{T_0}\int_t^{t+T_0} u_i\{x,y,z,t\}\,u_j\{x,y,z,t\}\,dt \tag{57}$$

The modeled Reynolds stresses are calculated as in RANS. At each time step, the velocity fluctuations squared are calculated, as well as the sum of the velocity fluctuations squared,

$$q^2 = \left(u'^2 + v'^2 + w'^2\right) \tag{58}$$

These variables are averaged over time. The resolved Reynolds stresses are added to the corresponding modeled Reynolds stresses for the total Reynolds stresses in the entropy generation calculations using the same equations used in analysis of RANS simulations.

5.5 Results and Discussion

All 3D simulations using LES models and IDDES were compared to DNS data. The results from these simulations are plotted and discussed here. All LES and IDDES simulations results show significant differences to that of DNS data for all variables. A comparison is made for the skin friction co-efficient C_f evaluated using the 3D LES simulation in OpenFOAM, LES and IDDES simulation using FLUENT to that from DNS data.

Figure 5.3 shows C_f values along the length of the flat plate evaluated from LES and IDDES simulations. The analytical laminar and turbulent profiles are also shown as a reference. The LES results from OpenFOAM simulations with all dynamic models and filtering function combination show similar results. The flow tends to stay laminar throughout the domain. The curve deviates from the laminar profile at $R_{e_x}^{0.5} = 450$ exactly where the DNS curve encounters transition to turbulence. However, the LES flow solution does not transition to turbulence. As suggested by Comte et al. [65], the SGS models are over-dissipative and lose turbulent kinetic energy, specified at the inlet, in a spatially growing boundary layer. Large-amplitude perturbations are introduced at the upstream boundary in order to correct for this over-dissipative nature of the SGS models for flat plate boundary layers.

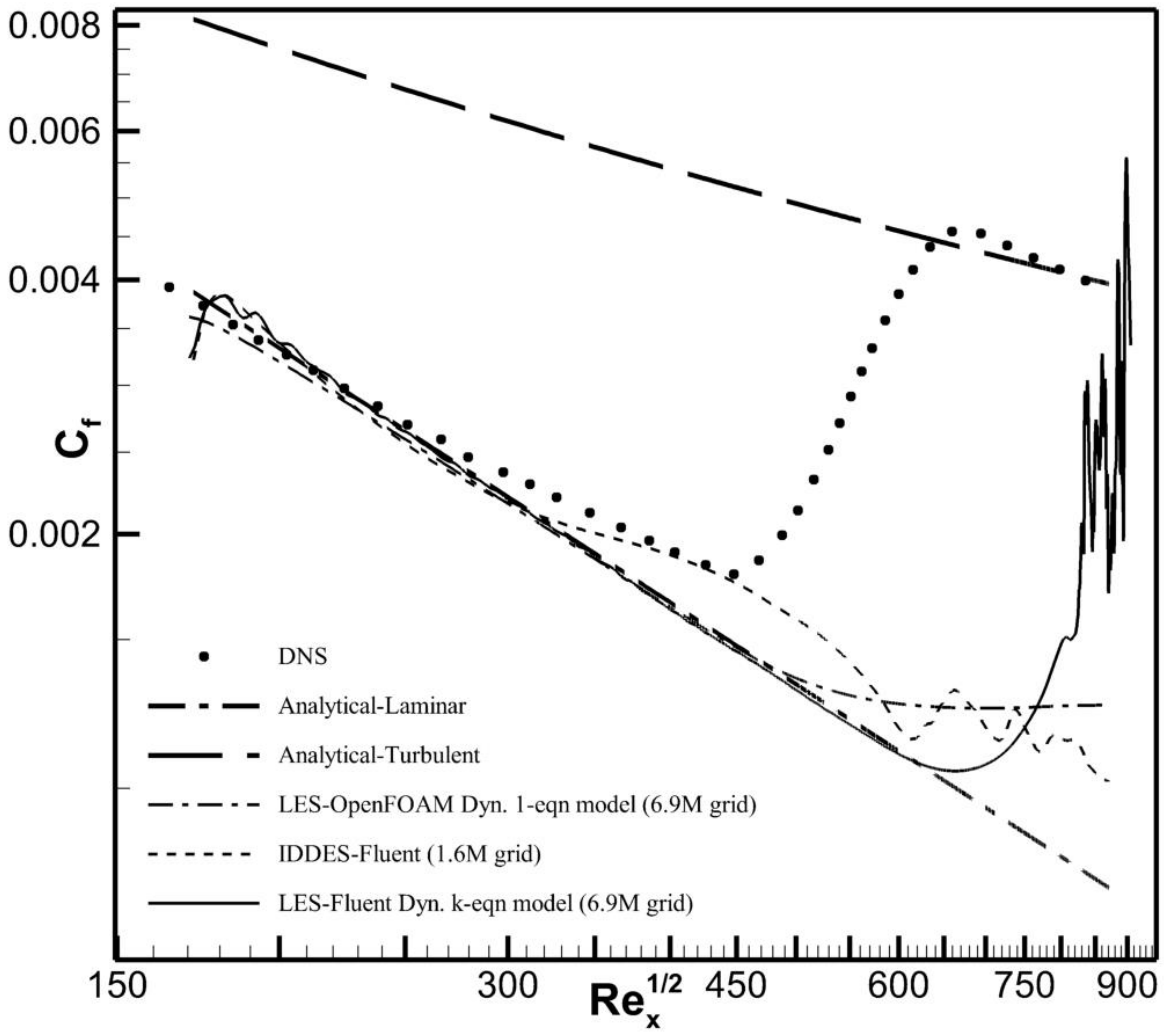

Figure 5.3 Skin Friction Coefficient C_f comparison for 3D ZPG simulations with DNS

A turbulent intensity inlet boundary condition was used for the OpenFOAM simulations. Existing inflow boundary condition available in OpenFOAM did not allow for specification of such fluctuations at the inlet. Attempts were made to implement a turbulent inflow boundary condition based on a vortex method as described in [71]. These attempts were unsuccessful on the local workstation while running a virtual Linux environment due configuration and software version problems. Therefore, LES models in OpenFOAM could not be simulated with a fluctuating inlet conditions.

ANSYS FLUENT incorporates two selectable methods to artificially fluctuate the mean inlet statistics and boundary condition specified using vortex method or a spectral synthesizer method. Simulations in FLUENT using the vortex method were unsuccessful due to setup and improper flow development in the domain. The IDDES and LES simulation results from FLUENT shown in Figure 5.3 were done employing the spectral synthesizer method.

IDDES results are considerably different from the DNS and both sets of LES simulations in magnitudes and trend. The flow is laminar initially until $R_{e_x}^{0.5} = 300$ and develops a fluctuating C_f profile downstream. As seen from Figure 5.3 LES simulation results from FLUENT using the spectral synthesizer method shows similar trend as seen from the DNS profile with a laminar region (until $R_{e_x}^{0.5} = 600$) and then transitions to turbulence downstream and reaches fully turbulent values near the outlet. It was seen that the LES results initially showed transition at around $R_{e_x}^{0.5} = 475$ after 1 flow through time. However, over time the transition location moved further downstream as seen in Figure 5.3. The LES simulation still exhibit the over-dissipative nature of the SGS models even with a fluctuating inlet.

This result indicates that although artificial fluctuation of the inlet profiles help in predicting transition, the overall magnitude and accuracy of the simulations are completely dependent upon the nature, frequency and magnitude of the fluctuations. The DNS simulations were carried out using an unsteady inlet profile based on the Orr-Somerfield and squire mode fluctuations. LES simulations with an exact fluctuating unsteady inlet as in the DNS study may result in more accurate and stable simulations.

The identification of coherent vortices is investigated on the basis of the Q-criterion as described by Dubief [72]. Q is the 'second invariant of the velocity gradient tensor.' The Q-criterion is employed as a flow visualization technique for CFD results. The Q-criterion (region where Q is positive) is a necessary condition for the existences of vortical features within a flow. Q-isosurfaces turn out to display very nice coherent vortices and is a commonly used tool in identification and visualization of vortical structures within a complex flow solutions. Detailed explanation, equations and proper use of Q-criterion can be found in [72].

Figure 5.4 shows the 3D Q-criterion within the flow field for the IDDES simulation. The figure qualitatively shows the streaks and spots in transitional flow as explained by Zaki in [44]. The figure shows initial laminar region with no vortical features, development of downstream streak line near beginning of transition and formation of turbulent spots further downstream closer to the outlet.

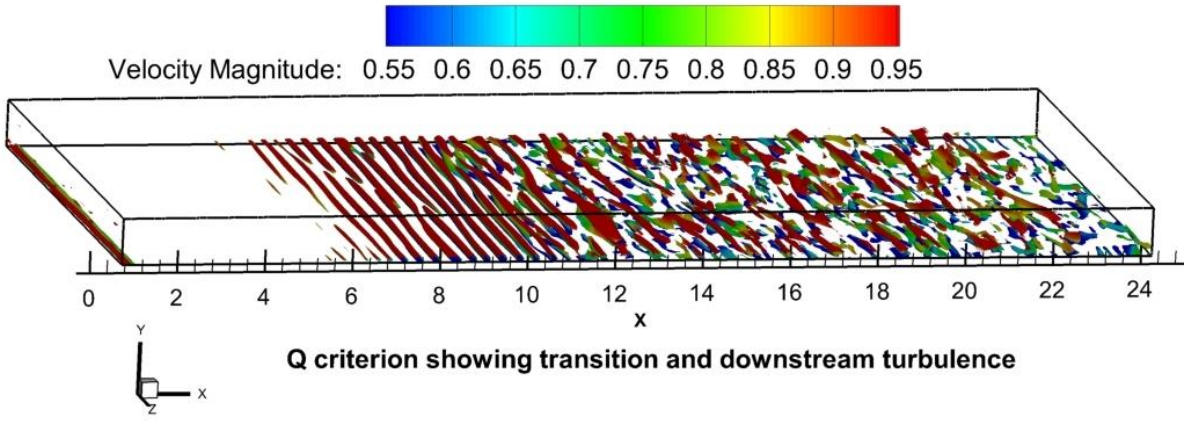

Figure 5.4 3-Dimensional Q-criterion showing development of flow colored by velocity magnitude (using IDDES, grid information)

The streaks and spots of transition and its development to higher turbulence within the spatially growing boundary layer as described by Zaki [44] are more clearly depicted and understood from Figure 5.5.

It shows, qualitatively, the three distinct regions: laminar, transition and turbulence, of a growing boundary layer over a flat plate.

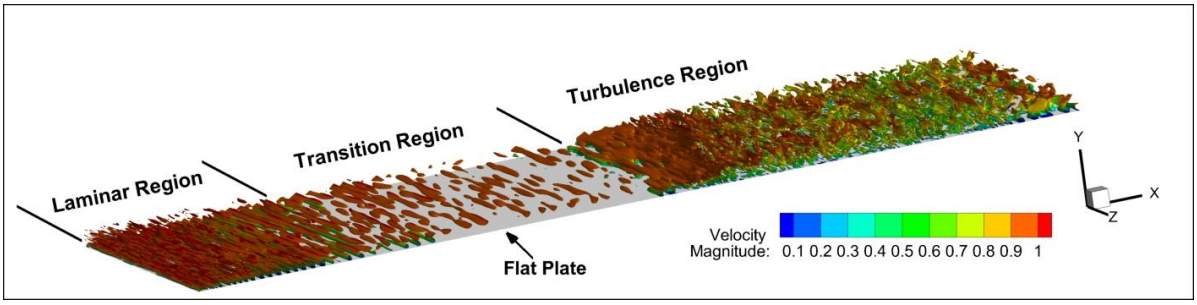

Figure 5.5 3D Q-criterion within the boundary layer showing 3 distinct regions over the flat plate from LES simulation using ANSYS FLUENT (6.9M grid set)

The laminar boundary layer region is not very clearly seen in the figure since they are being blocked by the vortical fluctuations generated within the freestream at the inlet above the boundary layer. The spanwise generated streaks can be seen near the beginning of the transition region.

The transition region is characterized by the two distinct features: the spanwise streaks and the turbulent spots. Further downstream the boundary layer grows and the flow becomes turbulent and hairpin vortices are generated near the outlet of the domain.

Figure 5.6 shows the velocity magnitude, x-velocity and y-velocity contours shown on 2-dimensional slices through the flow domain at 50% of total span, and a y-slice inside the boundary layer (2% of total height in normal direction).

The breakdown of the boundary layer from laminar to transition and to turbulence are seen clearly. The y-velocity contours show negative value contours within the turbulent region indicating a vortical characteristics of a hairpin vortex in the wall normal direction.

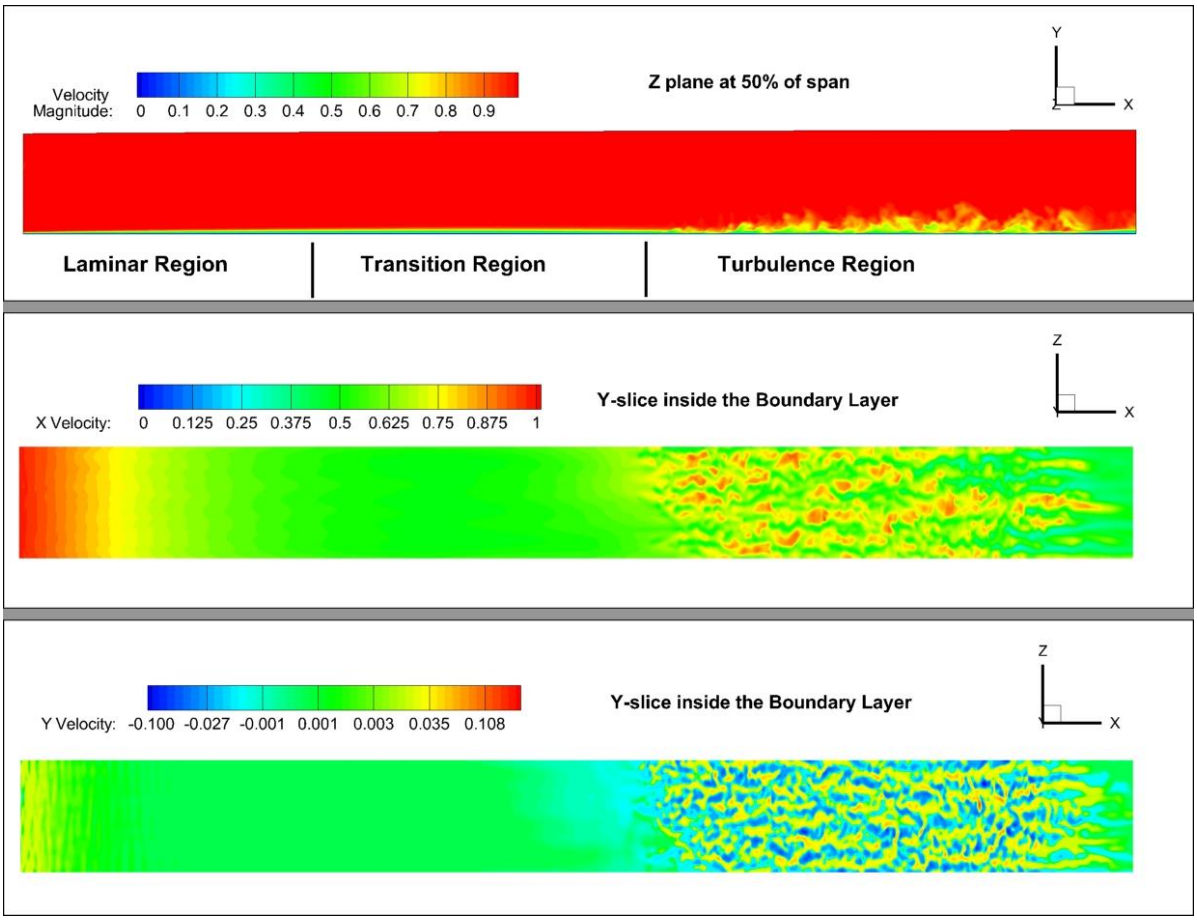

Figure 5.6 2-Dimensional views of the flow domain showing three regions of boundary layer flow using LES (6.9M grid)

To summarize, the LES and IDDES simulations qualitatively show the flow physics of a spatially growing boundary layer. However, the SGS models are overly-dissipative and are not able to be used for quantitative comparisons and application for wall bounded boundary layer flows. Such applications would require specification of very accurate custom boundary conditions depending on the flow being evaluated.

The development of accurate fluctuations at the upstream boundary are also not easily done and have limitations based on available computing resources and considerably increase the computational costs. However, further investigation, development and use of unsteady inlet conditions would result in more accurate comparisons and application of LES models to boundary layer flows.

Chapter 6: Conclusion and Future Work

This study evaluated the capability of various RANS models to predict entropy generation rates in bypass transitional boundary layer flows with and without pressure gradients. The results show significant improvements over the RANS results by Ghasemi et al. [18, 19] for all comparable models due to the employment of a much finer grid and more accurate inlet boundary conditions for velocity and turbulence structures.

Overall, the results from this study are more accurate and comparable to the DNS results than the results from Ghasemi for both ZPG and APG cases with respect to trends and magnitude for all corresponding RANS models except for slight under prediction of magnitude within the fully turbulent regime. Better grid resolution within the boundary layer also helps predict the approximate pointwise entropy generation rate profiles for adverse pressure gradient cases more closely to DNS than Ghasemi et al.

The results suggest that the k-ω 4 equation model predicts the boundary layer behavior and entropy generation more accurately than other RANS models for bypass transitional flows. All other models predict premature transition onset upstream of the location indicated from the DNS study. However, the k-ω transition 4 equation model also slightly over predicts the onset of transition based on the skin friction coefficient for the ZPG case and under predicts in the APG cases compared to DNS.

The capability of using different LES models to predict entropy generation rates for bypass transitional flows with and without streamwise pressure gradients could not be effectively evaluated within this study. The inherent over-dissipative nature of the SGS models and the specification of a more accurate unsteady fluctuations at the inflow boundary proved to be a major hurdle in completing the study.

In the future, the use of accurate unsteady hydrodynamic instabilities in velocity and turbulence structure profiles at the inlet may lead to more accurate CFD predictions for bypass transitional boundary layer flows using both RANS and LES models with varying pressure gradients [73]. The unsteady inlet statistics based on Orr-Somerfield and Squire modes as used in the DNS study would result in a more accurate and robust set of simulations.

LES models require higher inlet turbulence generation since the downstream kinetic energy dissipation is higher than the upstream turbulence kinetic energy production. This would be a key factor in future LES simulations for spatially growing flat plate boundary layer flows. Newer inflow conditions and improved dynamic non-equilibrium wall-model for large eddy simulation [43] are being developed for direct application to transitional boundary layer evaluations.

Further parametric studies could be performed to reveal and explain the noted trends of the entropy generation variables in the boundary layer using Large Eddy Simulations as suggested. LES models could be evaluated with a much finer grid within the boundary layer thereby eliminating any wall modelling and wall treatment limitations. Sensitivity of LES models to grid resolution and time step size could also be examined following the recent general framework for LES verification and validation proposed by Xing [49, 50].

References

[1] Bejan A, 1982, Entropy generation through heat and fluid flow, Wiley.

[2] Zaki T A, and Durbin P A. Mode Interaction and the Bypass Route to Transition, Journal of Fluid Mechanics, 2005, 531(1): 85-111.

[3] Walsh E J, Mc Eligot D M, Brandt L, and Schlatter P. Entropy Generation in a Boundary Layer Transitioning Under the Influence of Freestream Turbulence, Journal of Fluids Engineering, 2011, 133(6): 061203.

[4] Nolan K, and Zaki T. Conditional Sampling of Transitional Boundary Layers in Pressure Gradients, Journal of Fluid Mechanics, 2013, Under review).

[5] Ozkol I, Komurgoz G, and Arikoglu A. Entropy generation in laminar natural convection from a constant temperature vertical plate in an infinite fluid, Proceedings of the Institution of Mechanical Engineers, Part A: Journal of Power and Energy, 2007, 221(5): 609-616.

[6] Esfahani J, and Jafarian M M. Entropy generation analysis of a flat plate boundary layer with various solution methods, Scientia Iranica, 2005, 12(2): 233-240.

[7] Walsh E J, Nolan K P, McEligot D M, Volino R J, and Bejan A. Conditionally-Sampled Turbulent and Nonturbulent Measurements of Entropy Generation Rate in the Transition Region of Boundary Layers, Journal of Fluids Engineering, 2007, 129(5): 659-664.

[8] Nolan K P, Walsh E J, McEligot D M, and Volino R J. Predicting Entropy Generation Rates in Transitional Boundary Layers Based on Intermittency, Journal of Turbomachinery, 2007, 129(3): 512-517.

[9] Adeyinka O B, and Naterer G F. Experimental uncertainty of measured entropy production with pulsed laser PIV and planar laser induced fluorescence, International Journal of Heat and Mass Transfer, 2005, 48(8): 1450-1461.

[10] Adeyinka O B, and Naterer G F. Measured turbulent entropy production with large eddy particle image velocimetry, Experiments in Fluids, 2007, 42(6): 881-891.

[11] White F M, 2006, Viscous Fluid Flow, McGraw-Hill, Estados Unidos.

[12] Skifton R, Budwig R, McEligot D, and Crepeau J. Measurement of entropy generation within bypass transitional flow, Bulletin of the American Physical Society, 2012, 57(

[13] Skifton R, Budwig R, McEligot D, and Crepeau J. Measurement of entropy generation within bypass transitional flow, APS Meeting Abstracts, p. 19008.

[14] McEligot D M, Walsh E J, Laurien E, and Spalart P R. Entropy Generation in the Viscous Parts of Turbulent Boundary Layers, Journal of Fluids Engineering, 2008, 130(6): 061205.

[15] Spalart P R. Direct Simulation of a Turbulent Boundary Layer Up to Reθ= 1410, Journal of Fluid Mechanics, 1988, 187(1): 61-98.

[16] Spalart P R. Numerical Study of Sink-Flow Boundary Layers, Journal of Fluid Mechanics, 1986, 172(1): 307-328.

[17] Rotta J. Turbulent boundary layers in incompressible flow, Progress in Aerospace Sciences, 1962, 2(1-95.

[18] Ghasemi E, McEligot D, Nolan K, Crepeau J, Tokuhiro A, and Budwig R. Entropy Generation in a Transitional Boundary Layer Region Under the Influence of Freestream Rurbulence Using Transitional RANS Models and DNS, International Communications in Heat and Mass Transfer, 2013, 41(10-16.

[19] Ghasemi E, McEligot D, Nolan K, Crepeau J, Siahpush A, Budwig R, and Tokuhiro A. Effects of adverse and favorable pressure gradients on entropy generation in a transitional boundary layer region under the influence of freestream turbulence, International Journal of Heat and Mass Transfer, 2014, 77(475-488.

[20] McEligot D M, Walsh E J, and Laurien E. Entropy Generation In The Viscous Layer Of A Turbulent Channel Flow, 5th International Symposium on Turbulence, Heat and Mass Transfer, J. R. Wolf, ed., Idaho National Laboratory (INL).

[21] Abe H, Kawamura H, and Matsuo Y. Direct Numerical Simulation of a Fully Developed Turbulent Channel Flow With Respect to the Reynolds Number Dependence, Journal of Fluids Engineering, 2001, 123(2): 382-393.

[22] Krause E, Oertel H J, Schlichting H, Gersten K, and Mayes C, 2004, Boundary-Layer Theory, Springer.

[23] McEligot D M, Nolan K P, Walsh E J, and Laurien E. Effects of Pressure Gradients on Entropy Generation in the Viscous Layers of Turbulent Wall Flows, International Journal of Heat and Mass Transfer, 2008, 51(5-6): 1104-1114.

[24] Tsukahara T, Seki Y, Kawamura H, and Tochio D. DNS of turbulent channel flow at very low Reynolds numbers, Proceedings of the 4th International Symposium on Turbulence and Shear Flow Phenomena, pp. 935-940.

[25] Walsh E J, and McEligot D M. A New Correlation for Entropy Generation in Low Reynolds Number Turbulent Shear Layers, International Journal of Fluid Mechanics Research, 2009, 36(6): 566-572.

[26] Abe H, Kawamura H, and Matsuo Y. Surface Heat-Flux Fluctuations in a Turbulent Channel Flow Up to Reτ = 1020 with Pr = 0.025 and 0.71, International Journal of Heat and Fluid Flow, 2004, 25(3): 404-419.

[27] Hoyas S, and Jiménez J. Scaling of the velocity fluctuations in turbulent channels up to Re= 2003, Physics of fluids, 2006, 18(011702.

[28] Schlatter P, Brandt L, De Lange H, and Henningson D S. On streak breakdown in bypass transition, Physics of fluids, 2008, 20(101505.

[29] Brandt L, Schlatter P, and Henningson D S. Transition in Boundary Layers Subject to Free-Stream Turbulence, Journal of Fluid Mechanics, 2004, 517(167-198.

[30] Owen L D, Xing T, McEligot D M, Crepeau J C, and Budwig R S. Laminar and Transitional Boundary Layer Entropy Generation Over a Flat Plate Under Favorable and Adverse Pressure Gradients, ASME 2013 Fluids Engineering Division Summer Meeting, American Society of Mechanical Engineers, pp. V01BT16A005-V001BT016A005.

[31] Lardeau S, Ning L, and Leschziner M A. Large eddy simulation of transitional boundary layers at high free-stream turbulence intensity and implications for RANS modeling, Journal of turbomachinery, 2007, 129(2): 311-317.

[32] Lardeau S, Leschziner M, and Zaki T. Large Eddy Simulation of Transitional Separated Flow Over a Flat Plate and a Compressor Blade, Flow, turbulence and combustion, 2012, 88(1-2): 19-44.

[33] Monokrousos A, Brandt L, Schlatter P, and Henningson D S. DNS and LES of Estimation and Control of Transition in Boundary Layers Subject to Free-Stream Turbulence, International Journal of Heat and Fluid Flow, 2008, 29(3): 841-855.

[34] Sheikhi M R H, Safari M, and Metghalchi H. Large Eddy Simulation for Local Entropy Generation Analysis of Turbulent Flows, J. Energy Resour. Technol. Journal of Energy Resources Technology, 2012, 134(4): 041603.

[35] Huai X, Joslin R D, and Piomelli U. Large-eddy simulation of transition to turbulence in boundary layers, Theoretical and computational fluid dynamics, 1997, 9(2): 149-163.

[36] Ferziger J H. Direct and Large Eddy Simulation of Turbulence, JSMET Transactions of the Japan Society of Mechanical Engineers Series B, 2000, 66(2754-2763.

[37] Kornhaas M, Sternel D C, and Schäfer M, 2008, Influence of time step size and convergence criteria on large eddy simulations with implicit time discretization, Quality and Reliability of Large-Eddy Simulations, Springer, pp. 119-130.

[38] Sayadi T, and Moin P. Large eddy simulation of controlled transition to turbulence, Physics of Fluids (1994-present), 2012, 24(11): 114103.

[39] Sayadi T, and Moin P. Predicting natural transition using large eddy simulation, Center for Turbulence Research Annual Research Briefs, 2011: 97-108.

[40] Sayadi T, Hamman C, and Moin P. Direct numerical simulation of H-type and K-type transition to turbulence, Center for Turbulence Research Annual Research Briefs, 2011: 109-121.

[41] Sayadi T, Hamman C W, and Moin P. Direct numerical simulation of complete H-type and K-type transitions with implications for the dynamics of turbulent boundary layers, Journal of Fluid Mechanics, 2013, 724(480-509.

[42] Adrian R J. Hairpin vortex organization in wall turbulencea), Physics of Fluids (1994-present), 2007, 19(4): 041301.

[43] Park G I, and Moin P. An improved dynamic non-equilibrium wall-model for large eddy simulation, Physics of Fluids (1994-present), 2014, 26(1): 015108.

[44] Zaki T A. From streaks to spots and on to turbulence: Exploring the dynamics of boundary layer transition, Flow, turbulence and combustion, 2013, 91(3): 451-473.

[45] 2011, "FLUENT User Guide v14.0.0," ANSYS Inc.

[46] Xing T, and Stern F. Closure to" Discussion of'Factors of Safety for Richardson Extrapolation"'(2011, ASME J. Fluids Eng., 133, p. 115501), Transactions of the ASME-I-Journal of Fluids Engineering, 2011, 133(11): 115502.

[47] Xing T, and Stern F. Factors of Safety for Richardson Extrapolation, Journal of Fluids Engineering, 2010, 132(6): 061403.

[48] Wilson R V, Stern F, Coleman H W, and Paterson E G. Comprehensive Approach to Verification and Validation of CFD Simulations—Part 2: Application for RANS Simulation of a Cargo/Container Ship, Journal of Fluids Engineering, 2001, 123(4): 803-810.

[49] Tao X. A general framework for verification and validation of large eddy simulations, Journal of Hydrodynamics, Ser. B, 2015, 27(2): 163-175.

[50] Xing T, and George J. Quantitative verification and validation of large eddy simulations, ASME 2014 Ve- rification and Validation Symposium, ASME.

[51] Hinze J, 1975, Turbulence, McGraw-Hill Publishing Co., New York.

[52] 2011, "FLUENT Theory Guide v14.0.0," ANSYS Inc.

[53] Piquet J, 1999, Turbulent flows: models and physics, Springer Science & Business Media.

[54] Dewan A, 2010, Tackling turbulent flows in engineering, Springer Science & Business Media.

[55] Shur M L, Spalart P R, Strelets M K, and Travin A K. A hybrid RANS-LES approach with delayed-DES and wall-modelled LES capabilities, International Journal of Heat and Fluid Flow, 2008, 29(6): 1638-1649.

[56] Spalart P R, Deck S, Shur M, Squires K, Strelets M K, and Travin A. A new version of detached-eddy simulation, resistant to ambiguous grid densities, Theoretical and Computational Fluid Dynamics, 2006, 20(3): 181-195.

[57] Menter F R. Two-equation eddy-viscosity turbulence models for engineering applications, AIAA journal, 1994, 32(8): 1598-1605.

[58] Guide O U, 2011, "The OpenFOAM Foundation."

[59] Open C. OpenFOAM user guide, OpenFOAM Foundation, 2011, 2(1).

[60] Guide O U. Programmers Guide, JDT Core., retrieved from on Apr, 2011, 27(3.

[61] Germano M, Piomelli U, Moin P, and Cabot W H. Dynamic Subgrid-Scale Eddy Viscosity Model, Summer Workshop.

[62] Balaras E, Benocci C, and Piomelli U. Two-layer approximate boundary conditions for large-eddy simulations, AIAA journal, 1996, 34(6): 1111-1119.

[63] Wilcox D C, 1998, Turbulence modeling for CFD, DCW industries La Canada, CA.

[64] Smagorinsky J. General circulation experiments with the primitive equations: I. the basic experiment*, Monthly weather review, 1963, 91(3): 99-164.

[65] Comte F D, and Lesieur M. Large-eddy simulation of transition to turbulence in a boundary layer developing spatially over a flat plate, Journal of Fluid Mechanics, 1996, 326(1-36.

[66] Kim W-W, and Menon S. Application of the localized dynamic subgrid-scale model to turbulent wall-bounded flows, AIAA Paper No. AIAA-97-0210, 1997.

[67] Spalart P, Jou W, Strelets M, and Allmaras S. Comments of Feasibility of LES for Wings, and on a Hybrid RANS/LES Approach, Proceedings of the First AFOSR International Conference on DNS/LES.

[68] Owen L D, 2013, "SIMULATION OF ENTROPY GENERATION IN LAMINAR AND BYPASS TRANSITIONAL BOUNDARY LAYER FLOWS," Master of Science, University of Idaho, College of Graduate Studies.

[69] Hedges L, Travin A, and Spalart P. Detached-Eddy Simulations Over a Simplified Landing Gear, Journal of fluids engineering, 2002, 124(2): 413-423.

[70] Xing T, Bhushan S, and Stern F. Vortical and turbulent structures for KVLCC2 at drift angle 0, 12, and 30 degrees, Ocean Engineering, 2012, 55(23-43.

[71] Jørgensen N G, and Nilsson H. Implementation of a turbulent inflow boundary condition for LES based on a vortex method, A course at Chalmers University of Technology, 2012.

[72] Dubief Y, and Delcayre F. On coherent-vortex identification in turbulence, Journal of turbulence, 2000, 1(1): 011-011.

[73] George J, Tao X, Mceligot D M, Crepeau J C, Budwig R S, and Nolan K P. Entropy generation in bypass transitional boundary layer flows, Journal of Hydrodynamics, Ser. B, 2014, 26(5): 669-680.